Summer 2023

Polygonal Faults In The Austin Chalk: Invariance Of Scale From Mud Cracks To Polygons With Implications Of Structural, Geomorphic And Isotopic Data On Polygonal Fault Geometry And Origin.

Kun Shang
Southern Methodist University, kshang0818@gmail.com

POLYGONAL FAULTS IN THE AUSTIN CHALK: INVARIANCE OF SCALE FROM MUD CRACKS TO POLYGONS WITH IMPLICATIONS OF STRUCTURAL, GEOMORPHIC AND ISOTOPIC DATA ON POLYGONAL FAULT GEOMETRY AND ORIGIN.

Approved by:

_____
Prof. Robert T Gregory
Professor

_____
Prof. Brian W. Stump
Albritton Professor

_____
Prof. Matthew Hornbach
Professor

POLYGONAL FAULTS IN THE AUSTIN CHALK: INVARIANCE OF SCALE FROM MUD CRACKS TO POLYGONS WITH IMPLICATIONS OF STRUCTURAL, GEOMORPHIC AND ISOTOPIC DATA ON POLYGONAL FAULT GEOMETRY AND ORIGIN.

A Dissertation Presented to the Graduate Faculty of the

Dedman College

Southern Methodist University

in

Partial Fulfillment of the Requirements

for the degree of

Master of Science

with a

Major in Geology

by

Kun Shang

B.S., Geology, Southern Methodist University

May 13, 2023

ACKNOWLEDGEMENTS

I would first like to thank my advisor, Dr. Robert Gregory, for suggesting this research project and providing guidance throughout the entire process. I would also like to thank my committee members, Dr. Brian Stump and Dr. Matt Hornbach, for their continued support and assistance throughout the project that helped shape this thesis. Furthermore, I'd like to thank Dr. Ian Richards, Dr. John Robbins, Dr. Neil Tabor, and Dr. Rita Economos for their help in the field and laboratory. I'd also like to thank Dr. Robert Criss for providing valuable suggestions to my thesis and for participating in my thesis defense oral examination. Furthermore, I thank my friends and family for their unwavering support and encouragement. Lastly, I'd like to express my sincere gratitude to the faculty and staff of the Roy Huffington Department of Earth Science at Southern Methodist University for their dedication to provide a rigorous and stimulating academic environment. Their knowledge and expertise have been instrumental in shaping my research.

Shang, Kun B.S., Southern Methodist University

Polygonal Faults in the Austin Chalk: Invariance of Scale from Mud Cracks to Polygons with Implications of Structural, Geomorphic and Isotopic Data on Polygonal Fault Geometry and Origin

Advisor: Professor Robert Gregory

Master of Science conferred May 13, 2023

Thesis completed May 4, 2023

The Cretaceous Austin Chalk contains large numbers of fractures and normal faults whose orientations have been attributed to either regional stresses (e.g., the Balcones fault trend) or, by analogy with the mudrocks, to polygonal faulting resulting from compaction. In this study, we present geomorphic data, field study, and stable isotope data to support that the majority of these faults in North Texas are polygonal. Field-measured fault orientations suggest randomly distributed fault strikes, indicating a polygonal fault structure. Using geomorphologic data (topographic and DEM data) on stream orientations suggests that the polygonal fault patterns are best reflected in the headwater (1st or 2nd order) streams. The higher-order streams tend to reflect the down-dip direction of the chalk. Furthermore, to simulate the formation of polygonal faults, desiccation of ooze-like muds to produce mud cracks generates polygonal patterns with cracks having orthogonal, Y, non-orthogonal, and crossing intersections. Preliminary results suggest a compositional dependence for the distribution of intersection types and a relationship between thickness and polygonal area. Fault asperity, striated calcite veins, and host-rock chalk samples have δ18O values of $-9.5 < \delta^{18}O_{PDB} < -4.4$‰ and $-4 < \delta^{18}O < -3.5$‰, respectively. Assuming the seafloor temperature is ~21℃ from *Inoceramid* $-2.6 < \delta^{18}O < -2.3$, the trapped Cretaceous seawater fluid (~ −1.2 ‰) suggests precipitation between 30 and 65 ℃ with the veins having

oxygen isotope ratios consistently lower than those of the host-rocks. These faults were likely formed in the Late Cretaceous to Paleogene during compaction and dewatering, consanguineous with the deposition of the overlying sediments that predate the Oligocene/Miocene Balcones faults.

TABLE OF CONTENT

LIST OF FIGURES

CHAPTER 1

Introduction

The Austin Chalk is a Late Cretaceous sedimentary formation composed of coccolith, nannofossils, and microfossils interbedded with marl (Dravis, 1979). The Austin Chalk crops out along an arcuate belt extending from the southwest to the north following the inferred trend of the subsurface Quachita Thrust Belt. The chalk was deposited on the continental shelf bounded to the south by the Gulf Basin (figure1). Austin Chalk can be divided into three subunits with comparable thicknesses (Pessagno, 1969), which within Dallas County are the Atco member (60 m, lower Austin Chalk), composed of alternating thick chalk and thin, laminated marl; the Bruceville member (70 m, Middle Austin Chalk), composed of burrowed chalk and light-colored marl cycles; and the Hutchins (60m, Upper Austin Chalk) member which is composed of less regular chalk and marl cycles with some thick marl layers (Hovorka & Nance, 1994; Pessagno, 1969).

Within Dallas County, the Austin Chalk is crosscut by faults commonly contain calcite veins along asperities on the fault planes. The fault offsets ranging from less than a meter to tens of meters with the smaller offsets more commonly exposed in the limited outcrops. These normal faults were recognized as part of the Balcones fault system by some studies because of the NE-SW strike (Reaser & Collins, 1988; Reaser, 1961). However, some other studies recorded normal faults with random strikes and suggests that they were formed via compaction (Shuler, 1918; Collins et al., 1990; Watkins, 1954; Hayward, 1978). This implies that these randomly oriented faults are formed under uniaxial compaction, similar to the polygonal faults in the North Sea (e.g. Cartwright, 1994).

The Balcones Fault Zone is composed of en-echelon normal faults and extends from south Texas near Del Rio eastward to San Antonio, where it bends and extends northward through Dallas County (Collins and Laubach, 1990; Reaser, 1968;). In north Texas, faults within the Balcones fault zone strike subparallel to the Austin Chalk outcrop (Reaser, 1961). The highest Balcones Fault Zone density is to the south near San Antonio (Collins & Hovorka, 1997). Most movements within the fault zone occurred during the Early Oligocene and Early Miocene (Weeks, 1945), but some faults may also have been initiated as early as the Late Cretaceous and as late as Eocene (Hayward, 1978; Collins et al., 1990).

As an intraplate fault zone, its mechanism has yet to be fully understood. Still, the Balcones may be related to the subsidence of the Gulf basin and subsequent flexure of the sedimentary layers, as well as the influence of the subsurface Ouachita orogenic belt (Foley, 1926; Ferrill et al., 2017; Collins et al., 1990; Murray, 1961). To the east of the Balcones Fault Zone, the Mexia and Luling fault zones are usually associated with the deformation of the Jurassic salt dome (Weeks, 1945). However, such a mechanism is unlikely directly related to the Balcones fault zone to the west, as it does not directly overlie the salt.

Polygonal faults are layer-bound fault systems that were first discovered on the Paleocene to Middle Miocene age mudrock in the subsurface of the North Sea (Cartwright, 1994). They are characterized by their polygonal planform geometry and small throw (usually 10-50m). Such polygonal faults have been discovered in over 100 basins worldwide (J. Cartwright, 2011). These faults are nontectonic (i.e. no preferred tectonic orientation) and appear to be close to syndepositional which given typical depositional rates develop over millions of years (Goulty, 2008). Development of the polygonal faults is usually confined within clay-rich, fine-grained Early Cretaceous or younger sediments deposited in shallow continental seaway basins (Cartwright,

2011; Xia et al., 2022), but sometimes they can also be found in chalk or sand-size sediments (Antonellini & Mollema, 2015; Tewksbury et al., 2014). The dip angles of these faults are usually steep at the top and flatter on the bottom due to either compaction from increasing burial (Cartwright, 2011).

Despite many discussions, genesis mechanisms for polygonal faults are uncertain. The most cited mechanisms include: 1) differential compaction, 2) syneresis contraction of ooze resulting from fluid expulsion, 3) diagenetically induced shear failure, 4) density inversion, and 5) gravity sliding due to low coefficient of friction (Goulty, 2002; Goulty, 2008; Cartwright & Dewhurst, 1998; Cartwright, 2011; Henriet et al., 1991; Davies et al., 2009).

Planform geometry of polygonal fault systems varies greatly depending upon the types of intersections of the faults which may depend upon the lithology and its internal layering. These patterns are categorized by Lonergan et al. (1998) into four main types based on their linearity, spacing, and intersection angles. Orthogonal intersections dominate most maps in the North Sea, with fewer or no hexagonal intersections discovered. The tendency to form orthogonal intersections was discussed in previous literature, usually attributed to the alternation of the stress field by early-formed cracks, which force the later-formed fractures to intersect them orthogonally (Lachenbruch, 1962). Factors that affect polygonal fault geometry include lithology, stress state, and layer thickness (Cartwright, 2011).

In this paper, we studied the distribution of these faults in the Austin Chalk through field measurements of fault orientations analyzing geomorphic data. The benefit of using the geomorphic data is that it avoids the problem of limited accessibility to the exposed outcrops. Desiccation experiments simulated planform of fault patterns using unconsolidated sediments in the lab tests whether there is a scaling law between small-scale fractures (cm-scale), outcrops (m-

scale) and large-scale fault patterns (in the scale of km). The results support that two types of faults exist in the Austin Chalk Formation, which are polygonal, minor normal faults formed in shallow burial depth shortly after deposition, and large residual Balcones faults formed under regional stress. This study supplemented the work of E.Collins (2013), Collins et al (2014) by measuring additional $^{18}O/^{16}O$ and $^{13}C/^{12}C$ ratios ($\delta^{18}O$ and $\delta^{13}C$ values) of the calcite-filled veins between fault surfaces, Austin Chalk host rock, and *Inoceramid* fossils to constrain the initiation depth and temperature of the precipitation of calcite along fault planes.

CHAPTER 2

Methods

2.1 Fault Measurements and Controls on Drainage Orientation

To understand the distribution of normal faults within the Austin Chalk, strike and dip measurements were made on the faults in outcrops along creek beds or erosional escarpments (Figure 1). The outcrops are located in Dallas County and divided into three sections: (1) The western ridge like margin of the Austin Chalk escarpment near the contact with the Eagle Ford Shale; (2) White Rock Creek and its tributaries; and (3) The eastern margin of the Austin Chalk exposures near the contact with the Taylor Marl Formation. Using the 60 ft per mile gradient of the escarpment (Raney et al., 1987) and the thickness of each member, the spatial distribution of the upper, middle, and lower Austin Chalk can be inferred via a simple trigonometric relationship (figure 1). Field observations on the lithostratigraphy of the exposed outcrops further constrain inferred layer boundaries in an area of limited exposures. Additionally, historical measurements from previous studies on the minor faults within the Austin Chalk supplement the field data (e.g. Nance et al., 1994; E.Collins, 2013; Shuler, 1918).

While field studies allow direct identification of fault planes on the outcrop, limited accessibility of outcrops restricts the statistics of fault patterns and their distribution. To address this issue, the direction of streams over Austin Chalk outcrops facilitates the estimation of fault geometries, assuming differential erosion leads streams to follow the path of fractures suggested by some stream parallel fault traces in White Rock Creek near Anderson Bonner Park between Forest Lane

and LBJ 635 Freeway. Drainage patterns over the Austin Chalk from southwest Texas near Del Rio to North Texas near the Red River were traced on three different datasets, including the 1:24,000 USGS topographic maps, the Elevation Derivative for National Applications (EDNA) Watershed Atlas, and The National Map (TNM) database digital elevation maps (DEM) 30m resolution and 1 by 1 degree map scale. The EDNA data set is composed of streamlines extracted from the 30-meter resolution DEM derived through the national elevation dataset with a flow accumulation threshold value of 5000. Streamlines in the dataset are in the scale of kilometers, with headwater streamlines that extend only over hundreds of meters ignored. The 1:24,000 USGS topo maps are secondary products derived from various GIS databases and includes most visible streamlines on the satellite images. Streamlines were also derived from the DEMs using the hydrology toolbox in ArcGIS, and the stream order of these streams is calculated based on the definition in Strahler (1952), which defines order 1 stream as the outermost headwater, and the highest order stream as the stream near the mouth. The first-order streams (headwaters) were extracted as the third dataset.

2.2 Desiccation Crack Experiments

Experiments were conducted in the lab by drying materials with various lithologies, grain sizes, and layer thicknesses. In total, five different materials were used in the experiments, including (1) clay-rich fluvial over bank deposit collected in White Rock Creek floodplain, (2) eroded Austin Chalk powders with grain size greater than 75um and smaller than 2mm, (3) fine sand size quartz powder, (4) silt to clay size calcareous sediment and (5) bentonite clay. Experiments are prepared in the lab by mixing sediment and water in a nearly 1:1 ratio. To ensure the material is well mixed, a stirring rod and the ultrasonic bath are implemented in making the slurry to avoid gravity sorting of the solids. Then, the slurry is poured on a 27cm * 20cm polypropylene tray and dried in a room

at 25°C until the fracture pattern is fully developed. For some of the experiments, a Nikon D7200 camera with a 14mm lens took a picture every twenty minutes until fully desiccated. Fracture patterns formed in these experiments are quantified based on the shape and angle of fracture intersections and the average area of polygons that the mudcracks formed. Fracture intersections are divided into four types: the non-orthogonal intersection between two fractures, the orthogonal intersection between two fractures, the Y intersection between three fractures, and the cross intersection based on the number of fractures involved and the intersection angles between the fractures. The average area of the polygon is calculated by dividing the tray area by the number of polygons formed within the crack pattern, and the depths of cracks are calculated by measuring with a ruler.

2.3 Oxygen and Carbon Isotope Analysis

Selected Austin Chalk, sparitic calcite, and *Inoceramid* fossils supplemented the δ18O and δ13C measurements of E. Collins (2013; Collins et al 2014). Austin Chalk, calcite veins, and *Inoceramid* samples were collected from the Austin Chalk outcrop and measured in this study using the method of McCrea (1950). These samples were brought to the lab, selected, crushed, and reacted with orthophosphoric acid under 25 °C for at least 12 hours until fully reacted. The resultant carbon dioxide gas was then quantitatively extracted and analyzed on a dual inlet Finnigan MAT252 mass spectrometer by sample standard comparison with ratios converted to the delta notation:

$$\delta \equiv [\frac{R_{sample}}{R_{standard}} - 1]1000;\ -1000 < \delta < \infty$$

Where the *R*'s refer to the $^{18}O/^{16}O$ ratio or the $^{13}C/^{12}C$ ratio. For carbonates, the PDB (Pee Dee Belemnite) standard is the reference for carbon isotopes, and PDB or SMOW (Standard Mean Ocean Water) are the standards for oxygen. Conversion between the PDB and SMOW standards

are necessary for some temperature calculations. Using the definition of δ, the standard conversion equation for a sample reported with respect to one standard after analysis with respect to a second standard is:

$$\delta_{SMOW}^{sample} = \delta_{PDB}^{sample} + \delta_{SMOW}^{PDB} + \frac{\delta_{PDB}^{sample}\delta_{SMOW}^{PDB}}{10^3}$$

or

$$\delta_{SMOW}^{sample} = 30.86 + 1.03086\,\delta_{PDB}^{sample}$$

The value of the PDB standard with respect to SMOW depends upon the experimental values of the CO_2-water fractionation factor at 25 °C (Freidman and O'Neil, 1977) that range from 1.0407 to 1.0417. The Pee Dee Belemnite standard was correctly defined (Friedman and O'Neil, 1997) as "the δO^{18} value of the CO_2 produced by reaction of 100 percent H_3PO_4 with PDB calcite at 25°C is +0.22 per mil *relative to* CO_2 *equilibrated at 25°C with SMOW water."*

A paleotemperature scale for carbonates in PDB and small variations in seawater is:

$$T\ (°C) = 16.5 - 4.3(\delta_{calcite} - \delta_{water}) + 0.14\ (\delta_{calcite} - \delta_{water})^2$$

$$\frac{dT}{d\Delta} = -4.3 + 0.28(\Delta)$$

For small δ values of water on the SMOW scale, because the value used in the equation is the CO_2 value of that equilibrated with water measured with respect to SMOW, water values on the SMOW scale are compared against the CO_2 liberated through acid digestion of carbonates. Because the definition of PDB scale as the CO_2 liberated by the extraction process, the PDB value of the carbonate goes into the paleotemperature formula (e.g. Criss 1999). Each per mil of uncertainty in the Δ, the quantity $(\delta_{calcite} - \delta_{water})$ accounts for an uncertainty of ~ 4°C in the temperature. This

suggests uncertainty in the starting water during vein formation dominates the uncertainty in the temperature estimates.

With an estimate of ocean water, the oxygen isotope composition of the carbonate gives a paleotemperature. An alternative expression based upon exchange experiments is a calibration using the corrected fit of O'Neil et al. (1969) from 0 to 500 °C:

$$\Delta_{calcite-water} = 2.78 * (10^6\, T^{-2}) - 2.89$$

$$\frac{d\Delta}{dT} = \frac{-2 \times 2.78 \times 10^6}{T^3} = 0.21/degree\ at\ 298K°$$

where $\Delta = \delta_{calcite} - \delta_{water}$ both reported on the SMOW scale.

All of these temperature estimates are subject to the condition that the carbonates are not diagenetically modified once crystallized, i.e. the chalk represents the conditions in the water column where the plankton were living, the benthonic temperatures at the bottom of the seafloor, and thirdly, the temperature of the veins at time of precipitation. Collins (2013; Collin et al. 2014) used the measured values of the chalk and *Inoceramid* benthic fossils of primary aragonite to constrain the Cretaceous thermocline supporting the idea the chalk carbonate and pristine aragonite fossils have not been extensively modified by diagenetic processes.

The precipitation temperature of the vein calcite may also be calculated once the degree of openness, the water-rock ratio, and the isotopic value of precipitating fluid are known. In a closed system (analogous to a beaker filled with water and chalk), the water and rock ratio is based on the principle of mass conservation (Taylor. et al., 1974), which is formulated as

$$\frac{W}{R}_{closed} = \frac{\delta^f_{rock} - \delta^i_{rock}}{\delta^i_{H2o} - (\delta^f_{rock} - \Delta_{rw})}$$

This called the closed system water/rock equation with the superscripts f and *i* referring to the final and initial values and the Δ_{rw} is the fractionation at the precipitation temperature. A more realistic equation which represents the gradual infiltration of water (e.g. Gregory et al. 1989a) is called the open system water-rock equation:

$$\frac{W}{R}_{open} = \ln\left(1 + \frac{W}{R}_{closed}\right) = ln\left(1 + \frac{\delta^f_{rock} - \delta^i_{rock}}{\delta^i_{H2o} - (\delta^f_{raock} - \Delta_{rw})}\right)$$

Note if the final rock (in this case, the vein) only represents a small fraction of the rock, i.e. the vein and the rest of the rock is unaffected, then the initial and final fluid are essentially the same; the water/rock ratio is large. Another way to look at water/rock ratio with respect to vein formation following the analysis of veins in Richards et al. 2002:

$$\delta^{18}O_{vein} = \frac{W/R}{1 + W/R}(\delta^{18}O_{ocean} + \Delta_{cc-w}) + \frac{1}{1 + W/R}\delta^{18}O_{chalk}$$

fluid buffered rock buffered

The vein composition sees the pristine ocean water as $W/R \rightarrow \infty$ and the chalk composition as $W/R \rightarrow 0$. Vein- fluid systematics in δ-δ diagrams show the relationship above can be rewritten in terms of fluid flux and reaction rate, *u* and *k*, respectively (Richards et al. 2002):

$$\delta^{18}O_{vein} = \frac{u/k}{1 + u/k}(\delta^{18}O_{ocean} + \Delta_{cc-w}) + \frac{1}{1 + u/k}\delta^{18}O_{chalk}$$

Both *W/R* and *u/k* are dimensionless ratios. In the stable isotope literature (e.g. Gregory et al. 1989a), the parameter *u/k* is defined unit flow per unit of the representative elemental volume so that the units are inverse seconds. In hydrology and chemical engineering, fluxes and reaction rates are measured in mass per unit area per unit time. The ratio of fluid flux to reaction rate is still

dimensionless. By converting the fluid flux into volumes of water instead of mass, the flux rate has units of length, i.e. the water/rock ratio becomes an integrated flux by multiplying by the length scale of the flow.

Initially, the reaction rate, *k* in units of inverse seconds, is very slow at the surface so that the ratio of the flow (*u* in inverse seconds resulting from porosity reduction) to the isotope exchange rate is large, i.e. the first term dominates. With burial and a decline in the *W/R* or *u/k*, the fluids become ^{18}O-shifted towards the rock value or rock buffered (i.e. the veins give back the rock). When *u/k* is large, the system behaves as if the veins are precipitating from seawater at elevated temperature; the veins are depleted relative to the minimally exchanged host rocks. Thus, if the system is closed and rock-buffered, the isotopic composition of the vein can be calculated from the following equation (Gregory & Gray, 1994)

$$\delta_{vein} = \Sigma x_i \delta_i^0 + \varepsilon$$

where $\Sigma\, x_i\delta_i^0$ represents the weighted isotopic composition of the host rock where the x_i are mole fraction of each rock constituent and ε is the fractionation between the initial dissolution and final precipitation step, $\Delta^f - \Delta^i$. During the deep burial, ε does not vary much with the temperature change, and the variations in the delta values of veins will be small and insensitive to temperature. However, initially near the surface, if the reaction rate is low, the system will behave as if it is fluid-buffered, the isotopic composition of the water will remain relatively unchanged and the veins will have the maximum sensitivity to temperature. The fractionation between the veins and the fluids will be directly related to the precipitating temperature and hence the burial depth. When *W/R* or *u/k* is large:

$$\delta^{18}O_{vein} = \left(\delta^{18}O_{ocean} + \Delta^f_{cc-}\right) = \delta^{18}O^i_{cha} - \Delta^i_{cc-} + \Delta^f_{cc-} = \delta^{18}O^i_{chalk} + \varepsilon$$

Because the fractions decrease with increasing temperate $\varepsilon<0$ so that the contrast between unaltered, unreacted chalk and the vein is proportional to temperature change due to burial and hence the burial depth. The vein has lower $\delta^{18}O$ values than the unreacted host rock, and reflect the unexchanged initial fluid, in this case seawater.

CHAPTER 3

Results

3.1.1 Field Observations--Western Escarpment Margin

Two outcrops located on Mansfield Road and Rock Quarry Road were visited in this region. In Mansfield Road, the rocks are exposed as roadcuts located on the west side of the Cedar Hill quadrangle, and the GPS coordinates for this location are 32°35’22” N and 96°59’23” W. The exposed rocks are part of the Atco member, and the outcrop dimension is around 6 meters high and 20 to 25 meters long, orienting at ENE to WSW. E. Collins (2013) reports the contact between Eagle Ford Shale and the Austin Chalk in at the bottom of this roadcut. However, only Austin chalk was spotted at this location, and the exposed Eagle Ford Shale is covered. Only two faults with calcite veins were identified, and these faults are orientated at 006° and 156° with opposite dip directions. Along the asperities on the fault planes, calcite veins are present in layers, which suggests episodic development of the fault planes. Displacements on these faults are around several centimeters and the width of the veins are less than a centimeter.

Outcrops at the Rock Quarry Road are located in the Oak Cliff quadrangle, and the GPS coordinates are 32°45’08” N, 96°53’07” W. This outcrop is an abandoned rock quarry with rocks exposed on quarry walls in three sides of a rectangle that has the dimension of 1200m long, 200m wide, and 12m high. Faults are common in this location with at least eight fault planes that cut through multiple layers but have small displacements and numerous minor faults terminated within chalk layers(figure 2a). Calcite veins are commonly present on the fault planes and are usually

sparitic when the veins are thick (greater than 1cm) and are multilayered when veins are thin. Slickensides or striated surfaces are present between each growth event. Strikes of the faults suggest that they can orient in all directions. Rocks in this location are part of the Atco member with thick chalk and thin marl. Evidence of bioturbation activities such as burrowing were also spotted on this outcrop. Contact between the Austin Chalk and the Eagle Ford Shale is exposed on the bottom of the outcrop, which is covered by debris.

3.1.2 Field Observation—White Rock Creek

Austin Chalk exposures are distributed along the NW-SE trending banks along the strike of White Rock Creek riverbank and its tributaries. Rocks in this section are part of the Bruceville member, and the GPS coordinates for the northernmost and southernmost sites are 32°55'14" N, 96°46'37" W and 32°51'50.64" N, 96°45'09.70" W, respectively. Minor normal faults were commonly seen and formed in clusters. These faults can dip in both directions and sometimes intersect with each other (figure 2d). Fault planes flatten or reflect when approaching clay-rich layers and sometimes terminate within thick marl layers. Fault displacements are usually in the range of several centimeters up to one meter. Most of the observed minor normal faults are oriented in SW and NE directions, perpendicular to the direction of the exposures, but others are parallel or oblique to the bank of the creek. Calcite veins commonly exist between fault planes, and their morphologies are similar to those sparitic calcite veins found in Rock Quarry road outcrop. Fractures are also commonly present on outcrops along the White Rock creek. These fractures are usually randomly distributed but sometimes can also form rectilinear patterns. Unlike the fault planes, calcite-filled veins do not exist between the fracture surfaces, which suggests that they postdate the faulting and vein precipitation. Furthermore, a set of joints on the exposed Austin Chalk outcrop that parallels

the Caruth Creek---a branch of White Rock Creek, as well as White Rock Creek itself. This may suggests differential erosion along the joint directions also occurs.

3.1.3 Field Observation—Eastern Escarpment Margin

Two sites on the eastern escarpment margin, include the Spring Creek Natural Area and the One Eleven Ranch Park., with GPS coordinates 32°59'36" N, 96°42'11" W and 32°58'21.67" N, 96°37'32.35" W, respectively. Similar to the exposures along the White Rock Creek, these two sites are river cut outcrops along the SE trending Spring Creek and the Rowlett Creek. In Spring Creek, exposed rocks contain both the Hutchins and the Bruceville members. Outcrops are usually 5-10m high, with minor normal faults spotted on the Hutchins exposure(figure 2b, 2c). The steep riverbank limits accessibility to the outcrop. Hence, no close measurements and examinations were conducted. In One Eleven Ranch Park, the Hutchins unit is composed of a thick Chalk layer, with thin shale exposed along the riverbank. Similar to the Middle and Lower Austin Chalk, the exposure Hutchins member contains numerous normal faults with similar morphology as previously described. Measurements were conducted on ten minor normal faults orienting in the NNE-SSW direction and possibly one major fault dipping in the NNE direction with an offset greater than 5 meters.

3.1.4 Lithostratigraphy

Boundaries between the upper, lower, and middle Austin Chalk are inferred based on the layer thickness and gradient of the Austin Chalk in Dallas. Using the values discussed in the previous section, the boundary between the upper and middle members is calculated to be almost 5km from the eastern margin of the escarpment, and the boundary between the lower and middle members is about 8 km from the western margin of the escarpment. These lines categorize the outcrops in the eastern margins (One Eleven Ranch Park, Spring Creek Natural Area) as the Upper Austin Chalk

formation and set the Lower-Middle-member boundary between the Anderson Bonner Park and the Hamilton Park outcrops. The western margin of the Austin Chalk Escarpment is composed of a scarp, while the eastern side is a dip slope. Outcrops in the western and eastern margins are composed of chalk interbedded with shale, suggesting that they are part of the Atco and Hutchins members, respectively. However, the thick marl/chalk in the Anderson Bonner Park outcrop suggests that rocks at this location are part of the Bruceville member. Thus, the boundary between the upper and middle members might be further to the west.

3.1.5 Summary of Direct Measurements of Fault Planes

In summary, nine Austin Chalk outcrop sites were visited, and seventy-eight normal faults were measured. These minor normal faults, which have displacements less than a meter, usually formed in clusters and are distributed in all units of the Austin Chalk formation, similar to the observation from previous studies (Reaser & collins, 1988; Collins & Laubach, 1992). By inputting our data into rose diagrams in Stereonet11(Allmendinger, 2011) software, we found that our measurements suggest normal faults widely distributed in the NE-SW direction, with few faults striking in the NW direction. This dominance likely reflects the directional bias of the outcrops since many fault measurements were done along NW-SE orienting White Rock Creek and its branches, which as a result naturally leads to more exposure of NE-SW orienting faults. By plotting our data with those taken in previous studies together on rose diagrams and conducting stress inversion (Watkins, 1954; E. Collins, 2013; Shuler, 1918; Nance et at., 1994), we found that the true distribution of these faults are randomly distributed with isotropic horizontal stresses (figure 2). By conducting stress inversion with the matlab software package StressInverse, we noticed that maximum compressive stress is nearly vertical, while sigma two and three are indifferentiable and distributed over 360°. This supports the idea that these faults were formed under uniaxial stress instead of regional stress.

Hence, they are likely not part of the Balcones faults but instead polygonal faults, which formed via dewatering and compaction. Furthermore, fault planes flatten when they propagate from chalk-rich to clay-rich layers and usually die out within thick marl layers, indicating that they are syndepositional. The changes in dip angle reflect the changes in coefficient of friction between the chalk and clay.

3.2 Stream Orientations

On the EDNA stream maps, three hundred fifty-four measurements were done on the streamlines over the Austin Chalk outcrop in North and Central Texas. By plotting data on rose diagrams, streams are grouped in two preferred orientations: SE-NW at 120° and SSW-NNE at 10°. These two directions correspond separately to the downdip towards the Gulf of Mexico and the strike of the inferred Balcones faults. More detailed USGS topo maps of the exposed Austin Chalk outcrops in the north, south, and central Texas are also portrayed in figure 4. In North Texas, 545 measurements were taken on streams over Ellis County and 527 measurements were taken over Dallas County. Both rose diagrams show NE-SW as the most abundant direction, while streams in Dallas County are more randomly distributed. In Central Texas, 218 measurements were taken on the drainages over the exposed Austin Chalk outcrop between Waco and Austin. The results show that most drainages are oriented between 330° and 30°, and the most frequent orientation is 10°. In Southwest Texas, 172 measurements were taken on the streams between Brackettville and Uvalde. The results show that most streams are distributed in two groups of directions at N50°E and S30°E. First-order streams are extracted from the DEMs over the identical area as the USGS topo maps. The number of measurements taken in Dallas County, Ellis County, Central Texas, and South Texas are 527, 545, 174, and 130, respectively. Streams in these regions have similar rose

diagrams as those for the USGS topo maps, with small discrepancies reflecting the orientation of high-order streams (figure 5).

3.2.1 Comparison with Fault Data

All three datasets show that in large scale, many streams over the Austin Chalk are preferentially oriented in NE-SW direction from south to north Texas (figure 5). In the USGS topographic maps, by categorizing the streams into four sections from North to South Texas, it is noticeable that the NE orientating streams seem to be more N-NE in the Northern part of Texas while more eastward in South Texas. Such trend fits the inferred direction of the Balcones fault zone, which also parallel the regional strike of Austin Chalk. Therefore, streams in regional scale likely reflect the effect of differential erosion on large-scale normal faults or the strike parallel contrast in lithology. It can then be inferred that the Balcones faults may have the strongest impact on streams in South and Central Texas, where the fault density is the highest (Collins et al., 1990), and weaker effects on streams in Dallas County, where the Balcones Fault Zones may be absent.

Most drainage maps at large scale do not reflect the randomly oriented faulting pattern of the minor normal faults as we seen in the field. However, previous studies indicate that the direction of intermittent and ephemeral drainages may follow the direction of faults and fractures (e.g., Blakemore, 1939; Dallas Petroleum Geologists, 1941). To testify this, available faults are compared with high resolution drainage data in small scale (7.5 minutes quadrangles) at Cedar Hill, Lancaster, Waxahachie, and Midlothian.

3.2.2 Cedar Hill Quadrangle

In the Cedar Hill quadrangle, fifty faults were measured by Watkins (1954). These data show that the largest faults are in the 125°-130° direction, and the most frequent orientations, in general, are 60°-80° and 100°-125° directions (figure 6). Measurements taken by E.Collins (2013) in the same

area show two similar orientations that are subparallel with those in Watkins (1954), as well as an additional direction at 180°-190°. Comparing these fault orientations with drainage directions, we noticed that the N-S and NE-SW orientations are reflected in the USGS drainages, and all three orientations are reflected in the first-order streams.

3.2.3 Lancaster Quadrangle

Ingels (1956) measured the normal faults in the Lancaster quadrangle and found that major faults strike in the NE direction at N26°E to N48°E, subparallel to the inferred Balcones Fault trend. Joints are also located on the outcrop in this region, and their dominant strike trend is NE-SW, with a minor trend of NW-SE. Some locations also have a set of joints trend in the E-W direction, but this direction does not appear frequently. Compared with the fracture data, the USGS topo maps drainages, and the first-order streams contain streams oriented in NE-SW and E-W directions (figure 7). Both rose diagrams also have many streams oriented in nearly N-S direction, which likely reflects the direction of minor faults in this region.

3.2.4 Waxahachie and Midlothian Quadrangles

In the Waxahachie and Midlothian quadrangle, Nance. et al. (1994) measured the faults on the exposed outcrop in the tunnel of the superconducting supercollider and found that the NW direction dominates. On the other hand, the USGS topo map drainages and the first-order streams are dominated by NE trending steams, producing a completely different pattern (figure 8). This discrepancy is likely due to the sampling bias in fault measurements as mentioned by Nance et al. (1994). The actual fault pattern previous measurements on the joint and large (displacement greater than 10m) normal faults orientations (Nance et al., 1994; Read, 1957; Reaser & Collins, 1988) show that most joints and large normal faults strike NE-SE at 40°-50°, and drainage orientations

may be influenced more by the major normal fault and joint orientations than the minor normal faults.

3.2.5 Influence of Topography

Topography has crucial impact on the direction of streams in regional scale. In North Texas, stronger resistance of Austin Chalk to weathering than the Eagle Ford and Taylor formations makes the outcrop forms an escarpment with gentle slope on the east side and steep slope on the west side (Dallas Petroleum geologists, 1941). The slopes drive streams to flow in the downdip direction and show most obvious effect on the long, high order streams in EDNA water Atlas. However, such topographic effect drastically decreases in lower order streams.

3.2.6 Summary Stream Drainage Data

Our analysis suggest that directions of streams over the Austin Chalk outcrop are susceptible to the influences of the Balcones Faults zone, minor faults, joints, and topographic relief. Because the effect of minor normal faults are strongest on ephemeral headwaters, first-order streams over a region with relatively flat topography and minimum effect from the Balcones Faults may be the most consistent with field observed minor normal faults. This suggests that the rose diagram of first order streams over Dallas County should be most coherent with the distribution of minor normal faults among all the regions analyzed. This rose diagram shows the most randomly distributed pattern, which fits the field-measured faulting pattern and the polygonal fault hypothesis.

3.3 Desiccation Crack Experiments

Ten desiccation experiments were conducted on various materials relevant to the compaction of the Austin Chalk. Among these experiments, five were conducted on White Rock Creek over-bank mud deposits with different thicknesses to assess the effect of thickness on the fracture pattern.

Four of these experiments were conducted in a 27 cm by 20 cm polypropylene tray, and an additional experiment was dried in a 44.45 cm by34.29 cm tray to examine whether boundary effects affect the pattern as function of container size. The result shows that as the layer thickness decreased, the average area of the polygons decreased accordingly.

A set of naturally occurring mudcracks near White Rock Creek was also measured to estimate the relationship between the spacing and thickness in a larger scale. The dimension of these mudcracks is larger than those in lab experiments, with thicknesses in tens of centimeters to a meter and polygon area in the scale of square meters. Since these mudcracks were formed on over-bank sediments near White Rock Creek, the lithological composition of these sediments is almost identical as those used in the lab experiments. Plotting the measured field data on the graph illustrates that the polygon area for cracks in the scale of meters also increases as the crack depth gets deeper, and the relationship generally agrees with the lab experiments.

By plotting these two sets of data on a log-log scale plot, we noticed that the best-fit equation for the relationship between depth and area of polygon is $\log(y) = 1.93\log(x) + 2.6$, where y represents the average polygon area, and x represents the fracture depth (figure 9). The R^2 value for such correlation is around 0.98. Polygonal faults in the North Sea are also plotted on the graph by using 300m as its vertical extent and 750m as its horizontal dimension (Cartwright, 1994). The result shows that the relationship between the vertical extent of fractures and the polygon area is scale invariant from centimeter to kilometer scale in clay-rich sediment, i.e. seven orders of magnitude.

On the other hand, fracture patterns do not vary much with the change in the vertical extent of fractures (figure 10). Plotting the abundancy of each type of intersections into clustered columns show that all five experiments had orthogonal intersections (75°-105°) as the most abundant

intersection type and non-orthogonal intersections (0°-75°, 105°-180°) as the second most abundant (figure 11). The number of cross and Y intersections varied among experiments, but they were always much less abundant (2.6-10% of total number of intersections) than the orthogonal and non-orthogonal intersections. Furthermore, fractures in all four experiments are curvilinear with no preferred orientation so that poles to the fractions occupy all directions around the circumference of the stereo net. Also, no obvious shift in fracture pattern orientation occurred as sediment thickness changed.

Six experiments were conducted to examine the lithologic effect on the fracture pattern via mixing various materials in different proportions. In the first experiment, 53 g of bentonite was mixed with 433.85 g of Austin Chalk powder (i.e. 12% clay). After fully desiccating the material, the fractures crack the surface into polygons of various sizes, where the polygon size is greatest at the center and decrease to the left and right edges (figure 12). At the center, where the polygons are the largest, 53% of the intersections are orthogonal, 27% are non-orthogonal, and 17% are Y intersections. On the left side of the tray, 38% of the intersections are orthogonal, 41% are non-orthogonal, and 21 % are Y intersections (figure 13). Analyzing the grain size of the material shows that the center has more clay size sediments than the side, indicating that the percentage of bentonite in the center is higher. Therefore, adding bentonite to the Austin Chalk powder increased the percentage of orthogonal intersections.

Four experiments are also conducted by mixing calcite powder with different amounts of silica sand (figure 14). First, fracture patterns on pure calcite were examined by drying 296.48 g of calcite powder in the lab, and the fracture pattern was recorded. Then, 163.8 g of silica sand was added to the calcite in the first cycle (i.e. 65% calcite), and the tray was refilled with water for

desiccation. In the third cycle, 50g of silica sand was added to the mixture (i.e. 60% calcite) and desiccated again, and such a process was repeated for the fourth cycle by adding another 50 g of silica sand (i.e. 54% calcite). To ensure that lithology is the only variable involved, all the experiments were done on the same 27 cm by 20 cm tray and within the same room, where the temperature remained at 22 °C. The results show that as more silica sand is added, the percentage of orthogonal intersections decreases and the ratio of Y intersections increases accordingly (figure 15). On the other hand, the abundance of the cross and non-orthogonal intersections remains relatively constant. Another noticeable change in the fracture pattern is that the average polygon size decreases as the percentage of quartz sand increase, and the fracture depth also becomes shallower.

3.4 Oxygen and Carbon Isotope Values

Forty-seven samples were collected from the Austin Chalk outcrop and measured in this study, including three host rocks, seven *Inoceramid* fossils, and thirty-seven calcite-filled veins. The isotopic composition of these samples was measured relative to the PDB scale; $\delta^{18}O$ values of host rocks span from −3.0‰ to −4.0‰; calcite veins range from −4.4‰ to −9.4‰ with an average of −7‰, more depleted than the host rocks. Values for the *Inoceramid* fossils range from −3.0‰ to −4.5‰ similar to the value of host rock. This is in contrast to the study of E.Collins (2014), these *Inoceramid* were not checked for primary aragonite, and their range is the same as the host rock, implying recrystalliztion to calcite.

$\delta^{13}C$ values for the host rock and the calcite veins are similar, suggesting carbon isotopes are rock-buffered. The values for host rocks range from 2‰ to 2.2‰, and the values for vein calcites range from 1.5‰ to 2.3‰, except for one sample that has a value of 3.8‰. $\delta^{13}C$ values for the *Inoceramid* fossils measured in this study are relatively higher than the vein and host rock (figure

16), with the spread in the δ values ranges from 2.2‰ to as high as 4.7‰ probably the result of some interaction with metabolic products of subsurface methanogenic bacteria whose release ^{13}C enriched bicarbonate (e.g. Gregory et al. 1989b). These values are generally consistent with the result in E. Collins (2013).

Veins in Central Texas near San Antonio and Southwest Texas near Del Rio have similar $\delta^{18}O$ and $\delta^{13}C$ values to those measured in this study (Ferrill et al., 2020; Lee et al., 1997). In Longhorn quarry near San Antonio, Texas, multilayered calcite veinlets measured by Lee et al. (1997) show that the $\delta^{18}O$ values can range from −0.6 to −6.0‰ across the veins, while the sparitic, secondary veins can have value as low as −9.1‰. Lee et al. also measured the oxygen composition of the host rocks and host lithons, and their values are usually around −3.0‰. $\delta^{13}C$ of all the samples are usually between 1.0-2.5‰, except for some secondary veins enriched in carbon isotope ($\delta^{13}C$ = 13.1‰). Ferrill et al. measured the composition of host rock and veins on five faults located in Southwest Texas near Del Rio. In their measurements, four of the five faults have $\delta^{18}O$ values of calcite veins as low as –9.5‰ and –6.0‰ for the host rocks. The other fault has veins with oxygen composition ranging from –2.6‰ to –5.0‰ and chalk value around –3.0‰. $\delta^{13}C$ for most of the samples range from 0.5‰ to 1.5‰, except measurements on the calcite vein from the Langtry west fault, which has a value around –1.0 ‰.

3.4.1 Seafloor Temperature

Paleotemperature of the Cretaceous seawater can be potentially estimated via the paleotemperature scale for carbonates in PDB by using the following equation from O'Neil et al. (1969) corrected by Yapp (1979)

$$T\ (°C) = 16.5 - 4.3(\delta_{calcite} - \delta_{water}) + 0.14\ (\delta_{calcite} - \delta_{water})^2$$

In this equation, $\delta_{calcite}$ refers to the $\delta^{18}O$ values of the marine carbonates formed in Cretaceous, and δwater is the $\delta^{18}O$ value of Cretaceous seawater. Since Austin Chalk is mostly composed of calcareous nannoplankton, with some foraminifera, which live on the ocean surface, inputting the $\delta^{18}O$ of the chalk into the equation will give back the temperature of surface seawater if the bulk chalk is unaltered by diagenesis. On the other hand, because *Inoceramids* live on the seafloor, the $\delta^{18}O$ value of unaltered *Inoceramid* fossil (aragonite) will give back the temperature of seafloor. Assuming that the $\delta^{18}O$ value of seawater in the Cretaceous epicontinental seaway was −1.2‰, similar to the value in an ice-free globe, the calculated average precipitation temperature for *Inoceramid* fossils collected in this study is 29℃, above the average precipitating temperature for Austin Chalk host rock (figure 17). These calculated temperatures fail to show the temperature gradient within seawater column, which suggests that our *Inoceramid* samples are diagenetically altered. The $\delta^{18}O$ measured by E.Collins (2013) shows that aragonite *Inoceramid*s from the same region were precipitated at around 21℃ -22℃. Such values show decreasing temperature with depth in ocean and is within the range of the Late Cretaceous Gulf Coast seawater temperature reported by other studies (e.g. Meyer et al., 2018). Hence, we will use the values in E. Collins (2013) as a reference for the ocean floor temperature in this study; this is important for estimating the depth of vein formation using stable isotopes.

3.4.2 Source of Fluid

Variations in the $\delta^{18}O$ values of the calcite veins and the consistency of $\delta^{13}C$ values between calcite veins and chalk samples suggest that most of the calcite veins were precipitated under the influence of $\delta^{18}O$ of the fluid (i.e. they do not directly give back the rock composition), and the existence of veins with enriched and depleted $\delta^{13}C$ values relative to the Austin Chalk potentially implies precipitation from fluid with different origins with respect to bacterially-mediated reactions

(Gregory et al. 1989b) that affect carbon isotopes (E.Collins, 2013; Ferrill, 2020; Lee et al, 1997). The potential fluid sources include meteoric water, pore water, and seawater, and their isotopic composition may vary significantly at the several per mil scale. If the precipitating fluid is mostly Cretaceous seawater, the $\delta^{18}O$ of the fluid should be close to −1.2‰ (Criss, 1999) meaning that seawater is the global ocean in an "ice-free" global green house. On the other hand, the $\delta^{18}O$ value of the fluid should be positive if it originated as seawater-derived formation water that is ^{18}O-shifted, or if the seawater itself was enriched by evaporation in a more isolated sea, i.e. surface seawater itself can vary as a result of climate (Figure 21). More negative $\delta^{18}O$ values of seawater can result from different salinity-$\delta^{18}O$ correlations imparted by climate effects due to relative proportions of meteoric water inputs to open ocean seawater that result in brackish epicontinental seas (Figure 21). Lower ^{18}O veins can be simplistically interpreted as originating from low ^{18}O-meteoric water (Ferrill et al., 2020 and references therein).

Given the low permeability of chalk, meteoric water and seawater are unlikely to be the primary fluid source after burial since they can hardly penetrate into Austin Chalk formation unless there is some gravity drive for subseafloor or surface fluid flow. Thus, the most likely source of fluid might be pore water trapped in between intergranular spaces during deposition. Trapped pore water likely preserves the $\delta^{18}O$ of the trapped Cretaceous seawater during deposition. However, as the fluid exchanges with the surrounding host rock, its isotopic composition may vary, particularly when the exchange time and temperature increase.

3.4.3 Fluid Flux

Fluid flux of pore water through a layer can be calculated via the change in porosity and depth. Assume steady state compaction, the fluid flux can be calculated via the equation in Berner (1980)

$$flux = \int_0^X \phi \, dx - \frac{\phi_x}{1-\phi_x} \int_0^X (1-\phi) dx$$

where ϕ represents porosity, x represents depth, and ϕ_x is the value of porosity when it becomes almost invariant on quasi-steady state with depth. For Austin Chalk, we use 0.3 as the value of ϕ_x since this is the lowest porosity that can be reached by mechanical compaction (Croizé et al., 2013). Hence, assuming that the initial porosity is 0.8, and 20% of the porosity reduction occurs in the upper 200 meters (Schlanger & Douglas, 1975), the porosity can be written as a function of depth in the following equation based upon empirical observations:

$$\phi = 0.5exp(-0.0025x) + 0.3$$

Thus, the flux equation becomes

$$flux = \frac{0.5exp(-0.0025x)}{-0.0025} + 0.3x \Big|_0^X - \frac{0.3}{1-0.3} * (x - \frac{0.5exp(-0.0025x)}{-0.0025} - 0.3x) \Big|_0^X$$

This equation suggests that total flux through a layer when it has been buried to 1000 m is around 285 m^3/m^2. Given that the estimated vein to chalk ratio in outcrop of the Austin Chalk is less than $1X10^{-3}$ (E.Collins, 2013), the total fluid to vein ratio may be as high as 10^5, comparable to the solution/vein ratio calculated by Lee & Morse (1999). This suggests that vertical flux alone is sufficient to explain the amount of calcite veins in the Austin Chalk Formation. However, from the analysis of section 2.3, the integrated flux would only give a *u/k* of 285 divided by the length scale 1000 meters, or 0.3 or only 23% fluid buffered. Similarly, if the representative volume is the volume of veins, the 0.3 may have to be multiplied by 10 to 100 (Collins, 2013). This is a minimum estimate because interconnected porosity at shallower depth provides additional flux of fluid that may swamped the uniform upward flow from the model of Berner (1980).

CHAPTER 4

Discussion

4.1 Distribution of Polygonal Faults and its Relationship with the Balcones Faults

Our results and the previous studies (e.g. Reaser, 1961) suggest that two sets of faults exist within the Austin Chalk formation in Texas: (1) NE-SW orienting large displacement normal faults that are part of the Balcones fault system and (2) Polygonal faults that can strike in all directions. Similarly, Ogiesoba et al. (2015) found polygonal faults distributed within the top of the Austin Chalk Formation using diffraction imaging in the Maverick basin. Therefore, the occurrence of polygonal faults in Austin Chalk in both North Texas and Southwest Texas suggests that polygonal faults may commonly exist within the Austin Chalk formation rather than being limited to a particular area.

The field study of the polygonal faults in the Austin Chalk shows no evidence of stress anisotropy between sigma 2 and 3 during the genesis of these faults. In contrast, the N-NE direction of the Balcones faults suggests that the least horizontal stress points toward the Gulf Coast (Zoback & Zoback, 1989). Thus, the Balcones and polygonal faults are likely to form at different times. We propose that the polygonal faults predate the Balcones faults because they are curvilinear and layer-bounded and hence most likely initiated syndepositionally during the Late Cretaceous. On the other hand, most fault movement within the Balcones fault zone occurred during the late Miocene to Oligocene (Weeks, 1945; Collins et al., 1990). These faults may be initiated by exploiting the preexisting weakness created by the polygonal faults (figure 18). Furthermore, the uniform stress regime revealed from the polygonal fault pattern likely only exists right after deposition before sediments become fully compacted, indicating that they formed soon after deposition. Additionally,

polygonal faults are believed to be associated with the dewatering of sediments, which mostly occurs at shallow depths under mechanical compaction.

4.2 Geothermal Gradient

The inferred geothermal gradient using the geothermal map made by Blackwell (2011) shows that the modern heat flow over the Austin Chalk formation outcrop varies from 45 to 75mw/m^2. These heat flux values can be converted to the geothermal gradient via the equation

$$H = \lambda \frac{dT}{dZ}$$

where λ represents the thermal conductivity of the rocks. Given the average thermal conductivity in Gulf Coastal Plain is around 2.3W/m°C (Nathenson and Guffanti, 1988), the calculated geothermal gradient varies from 20-32°C/km. Thus, if δ_{fluid} is seawater and its value −1.2‰, most of the calcite veins suggest precipitation between 600m and 1.6 km (figure 19).

4.3 Variation in Isotopic Composition of Fluid

Variation in the $\delta^{18}O$ composition of the calcite veins exceeds that of host rock Austin Chalk samples, suggesting that these veins were not precipitated under rock-buffered condition. As discussed earlier, fluid compositions may have important implications on the precipitating temperature of the calcite veins, as determined by the fractionation factor equation sensitivity to the choice of the initial fluid changing the temperature of 4-5℃ for each per mil change in the initial fluid. In Austin Chalk, source of the fluid for calcite veins is most likely to be pore fluid which initially originated as Cretaceous seawater on the interior seaway, in which the isotopic composition may vary depending on the amount of influx of fresh water, glacial cycles, and the amount of evaporation (figure 20). The $\delta^{18}O$ of seawater at the western interior seaway in the study area can be as low as the modern Dallas precipitation ($-5‰ < \delta^{18}O < -4‰$; Gregory and Ferguson,

2004) and as high as 1‰ from water current Gulf of Mexico waters. Assuming vein precipitation under fluid-buffered conditions, this range of seawater may result in variation in the precipitating temperature of the calcite veins for as much as 24-30 ℃ (figure 21).

Besides variation in seawater value, the $\delta^{18}O$ of the fluid may also be altered through chemical reactions with the chalk and volcanic ash, and the influx of formation water. Influence of volcanic ash weathering on the δ_{fluid} in the Austin Chalk formation was previously mentioned by E.Collins(2013), where she showed that the effect of volcanic ash alteration could be estimated by the following equation assuming three components, closed system

$$X_{wf}\delta^{18}O_{wf} + X_{clay}(\delta^{18}O_{wf} + \Delta_{clay-wa}\quad) = X_{wi}\delta^{18}O_{wi} + X_{ash}\delta^{18}O_{as}$$

In this case, assuming the weathering equation can be written as

$$CaAl_2Si_2O_8 + 2H_2CO_3 + H_2O = Al_2Si_2O_5(OH)_4 + Ca^{2+} + 2HCO_3^{2-}$$

if the fractionation between clay and water is 20‰, the initial watern$\delta^{18}O$ varies from −1 to −4‰, and the $\delta^{18}O$ of the volcanic ash is similar to that of typical igneous rocks, which is around 7‰ in SMOW (Taylor, 1968), the shift in the fluid composition can be potentially calculated given that the Austin Chalk formation contains 10% of ash by volume and all the ash was weathered into clay during mechanical compaction (porosity reduced from 0.7 to 0.3). By solving mole fractions X_{wi}, X_{wf}, X_{ash}, and X_{clay} under different initial condition, $\delta^{18}O$ of water can be depleted by 0.41 to 0.93‰, which corresponds to 1 to 4℃ of temperature underestimation, an uncertainty less than that from the initial fluid composition.

Effect of chemical reactions with the host rocks on the composition of fluid and temperature can be demonstrated via solving the Δ with respect to the water rock ratio equation, which is

$$\Delta_{cc-} = \frac{1}{u/k}((1+u/k)\delta^{18}O_{vein} - \delta^{18}O_{cha}) - (\frac{u}{k})\delta^{18}O_{ocean}$$

As $u/k \to \infty$,

$$\Delta_{cc-w} \approx \delta^{18}O_{vein} - \delta^{18}O_{ocean}$$

As $u/k \to 0$,

$$\Delta_{cc-w} = (\delta^{18}O_{vein} - \delta^{18}O_{ocean}) - \frac{1}{u/k}\delta^{18}O_{chalk} \quad \text{indeterminant}$$

with the last term blowing up so that $\Delta_{cc-w} \to -\infty$ or indeterminant because Δ_{cc-w} must go to 0 as T becomes large, i.e. under rock-buffered conditions for a monomineralic rocks and vein, the vein reflects the rock composition:.

$$\delta^{18}O_{vein} = \frac{u/k}{1+u/k}(\delta^{18}O_{ocean} + \Delta_{cc-w}) + \frac{1}{1+u/k}\delta^{18}O_{chalk}$$

$u/k \to 0$:

$$\delta^{18}O_{vein} = \frac{1}{1+u/k}\delta^{18}O_{chalk} = \delta^{18}O_{chalk}$$

Based on this equation, given that the $\delta^{18}O$ of a calcite vein is 23‰ in SMOW and that for the initial fluid and chalk are −1.5‰ and 27‰, respectively, variation in Δ from rock-buffered (u/k = 0) to fluid-buffered (u/k →∞) can be calculated. If u/k is infinity, Δ equals the difference between $\delta^{18}O_{vein}$ and $\delta^{18}O_{ocean}$, which directly gives back a temperature of 45°C and the $\delta^{18}O$ for the final fluid remains unaltered. Whereas as u/k decreases to less than 0.8, Δ decreases accordingly to a value less than 20, which result in an unreasonably high temperature of greater than 75°C.

Lastly, influx of ^{18}O-enriched formation water into the layer will enrich the precipitating fluid. Given that the calculated total flux is on the scale of hundreds of m^3/m^2, such influence may be nontrivial. Ferrill et al. (2020) and Lee et al. (1997) examined the homogenization temperature of fluid inclusion and isotopic composition of calcite veins within the Austin Chalk formation and concluded that the source fluid is hot formation water with positive $\delta^{18}O$ values. In these studies, homogenization temperatures of fluid inclusions range from 51℃ to as high as 100℃, indicating a fluid with a $\delta^{18}O$ as high as 6‰ and precipitation depths up to 2 to 3 km, which contradicts the idea of syndepositional polygonal faults. The same veins have hydrocarbon fluid inclusions that may imply even higher temperature, calling into question whether any of the fluid inclusions are primary.

4.4 Interpretation of Isotopic Data

Since field observed faults show evidence of shallow burial (e.g. randomly oriented strikes, truncations and listric fault planes), this work supports the interpretation of E.Collins (2013), which states that the veins were initially precipitated at very shallow depth from trapped seawater. Retrograde solubility of calcite favors dissolution over precipitation in shallow depth. These early formed veins were most likely precipitated within the first kilometers of burial.

Evidence that may support the idea of precipitation from a fluid with enriched seawater composition is the existence of calcite veins with more enriched $\delta^{18}O$ values than the chalk. Lee et al. (1997) recorded oxygen isotope data on a multilayered calcite vein with consistent $\delta^{18}O$ PDB values around −0.6‰, i.e. enriched relative to the chalk predominantly precipitated in warmer surface waters, which they concluded resulted from precipitation from the deep, ^{18}O-shifted fluid that fluxed into the Austin Chalk formation. Fluid would have to be enriched in $\delta^{18}O$ by at least 3‰, alternatively, this $\delta^{18}O$ shift requires the bottom water temperature to be much lower by 10°C.

A possible explanation for the fluid inclusion data in the previous studies is that the fluid inclusions are associated with the initiation of the Balcones faults, which occurs at much greater depth than the polygonal faults. Fluid inclusion microthermometry from previous studies was done on samples collected from south Texas, where the Balcones faults are more prominent. It is unknown whether fluid inclusion from samples in North Texas will show similar high homogenization temperatures, but also similar to South Texas, both water and hydrocarbon inclusions were observed in a composite vein from the Atco in Dallas County. Calcite veins that contain fluid inclusion usually have very depleted $\delta^{18}O$ values , with some as low as −9.5‰. If the hypothesis is valid, these veins were likely precipitated neither in fluid-buffered nor rock-buffered conditions since the fluid shows influence from the rock composition, yet the depleted oxygen isotope composition of calcite veins is likely affected by higher temperature of formation.

Multilayered calcite veins discovered on the outcrop of Austin Chalk formation have veinlets parallel to the slip surface and have similar morphology as crack-seal veins, indicating that they are formed by diffusion under rock-buffered conditions. To examine whether these veins are truly rock-buffered, we measured the isotopic composition of a multilayered vein and its wall rock collected from the Atco unit outcrop at Rock Quarry Road. This vein has a steep dip angle (~80°) with a $\delta^{18}O$ value of 25‰ on the SMOW scale. The $\delta^{18}O$ of the wall rock right next to the vein is 27‰. Based on the water-rock ratio equation and the calcite water fractionation equation, we can estimate the water-rock ratio via

$$\mu/k = \frac{\delta^{18}O_{chalk} - \delta^{18}O_{vein}}{\delta^{18}O_{vein} - \delta^{18}O_{ocean} - (2.78 * 10^{6}T^{-2} - 2.89)}$$

$$\mu/k = \frac{27 - 25}{26.2 - (\Delta < 26.2)}$$

The result, using $\delta^{18}O_{ocean} = -1.2‰$, suggests that precipitation temperature should be higher than 36℃, the temperature at which *u/k* blows up when $\Delta = 26$. When temperature increases just 10 °C, Δ decreases with μ/k eventually becomes less than 1. The system becomes closer to rock-buffered, $1/(1+u/k.) > 0.5$. The vein precipitation becomes indeterminate for temperature as $u/k << 1$. thus, the crack-sealed calcite veins need to precipitate at over 45℃ for this particular example because the crack seal mechanism favors rock buffered conditions (Gray et al. 1991).

4.5 Possible Mechanisms for The Origin of Polygonal Faults

One of the possible explanations for the origin of polygonal faults is that the shear failures can be diagenetically induced via grain dissolution (Cartwright, 2011; Shin et al., 2008). However, given the low percentage of clay within the Austin Chalk formation, it is hard to consider such a mechanism as a major factor. Furthermore, the retrograde solubility of calcite and the high carbonate content within the chalk suggests that small amounts of calcite dissolves during the initiation of polygonal faults. Thus, the stresses are also unlikely to be altered by the dissolution of calcite.

Syneresis is another proposed mechanism to explain polygonal faulting and the associated volumetric contraction, which involves spontaneous contraction for gel-like material due to the flocculation of clay particles(Cartwright & Dewhurst, 1998). However, the Austin Chalk formation is mostly composed of calcareous oozes, which are unlikely to flocculate. Hence syneresis is unlikely to have a dominant effect.

Overpressure of pore fluid was also proposed as an important mechanism for developing the polygonal fault system (Cartwright & Lonergan, 1996; Tewksbury et al., 2014). Since the Austin

Chalk has low permeability and high porosity, this mechanism may significantly influence the initiation of faulting. Moreover, Tewksbury et al. (2014) argue that the very steep fault dips are most likely achieved by increasing pore fluid pressure. We observed similar steep fault planes (~80°) in the outcrop. Hence, the same argument is applicable in supporting the importance of overpressure in the Austin Chalk formation. However, as we mentioned previously, multilayered veins with very enriched $\delta^{18}O$ recorded by Lee et al. (1997) may indicate fault initiated near the surface, and it is not sure whether sufficient pore pressure can be built at a very shallow depth to produce faulting.

Lastly, differential compaction due to the chemical diagenetic process can account for polygonal faults with siliceous succession (Davies et al., 2009). However, it is unlikely that such a mechanism is responsible for the polygonal faults observed in the Austin Chalk formation, which consists mainly of calcareous sediments rather than siliceous succession. Furthermore, differential compaction hypothesis predicts folding along with faulting, but even in areas with high densities of faults, the presence of folding is scarce in the field.

Previous studies also proposed that the low coefficient of friction largely controlled the propagation of faulting (e.g. Goulty, 2001). Based on this principle, the stress state of the Austin Chalk formation under burial is estimated using burial depth, Poisson's ratio, and fluid volume. A uniaxial compression environment is assumed in this calculation, and the reason that such a hypothesis is valid is that the stress inversion result shows nearly indifferentiable σ_2 and σ_3, and $\sigma 1$ is in the vertical direction. The ratio between horizontal and vertical stresses can be calculated by the equation

$$K_0 = \frac{\sigma'_H}{\sigma'_V} = \frac{v}{1-v}$$

Where v is the Poisson's ratio. To initiate the faults via compaction, Goulty(2001) suggests that must satisfy the following relationship with the effective stress ratio

$$K_0 \leq \left(\sqrt{1+\mu^2} - \mu\right)^2$$

Where μ represents the friction angle, the Poisson's ratio, peak friction angles, and residual friction angles for Austin Chalk are 0.21, 38°, and 37°, respectively (Medetbekova et al., 2022). These values give K_0 slightly greater than the effective stress ratio in the Austin Chalk formation, and hence suggesting that faults stop propagating once Austin Chalk been diagenesis into the current stage. However, friction angle calculated based on the average dip of field measured fault plane, which is 58°, will result in a friction angle of 26° when faults were initiated, a number more consistent with granular material. The effective stress ratio calculated from this friction angle is 0.458, much larger than K_0. Thus, low coefficient of friction may allow the growth of polygonal faults in the initial stage, and as chalk undergoes diagenesis, the friction angle increases, and the fault growth stops when K_0 value surpasses the value of the effective stress ratio. However, for uncemented calcareous oozes, it is suggested that the Poisson's ratio value range from 0.49-0.41 in the first kilometer, similar to that of terrigenous clay (Hamilton, 1979). These values suggest a very high K_0, and to explain the fault initiation with only the coefficient of friction, μ value must be lower than 0.186 to 0.02, numbers more consistent with clays.

4.6 Implications of Mudcrack Experiments on the Pattern of Polygonal Faults

Our lab experiments suggest that on the scale of centimeters to meters, the most important factors in controlling the fracture pattern of mud cracks are the lithology and grain size. Similar variation also exists in the polygonal fault systems. For example, in the North Sea, lithological data and horizon maps from Dewhurst et al. (1999) and Lonergan et al. (1998) show that in block 21/14,

tiers with low clay content and high grain size have curved patterns with a broad spread of intersection angles. Tiers with high clay content and fine grain size have mostly orthogonal intersections. Furthermore, in the Khoman Chalk, located in western Egypt, polygonal faults form clusters that intersect orthogonally (Tewksbury et al., 2014). Therefore, this similarity may suggest that lithology is a scale-invariant factor that can influence the fracture pattern. In this way, the lack of hexagonal pattern in polygonal fault systems, as noticed by Lonergan et al. (1998) in the North Sea, can be explained by the fact that hexagonal pattern appears only in sediments with extensive amounts of coarse-grained sand materials and most polygonal faults only occur in clay-rich sediments or fine-grained materials with pronounced layering. Furthermore, since the Austin Chalk is dominantly composed of calcareous nannofossils with disc-like geometry (Corbett et al., 1987), we would expect that the polygonal fault system would have a pattern dominated by orthogonal intersections.

A possible mechanism that may explain the geometric variations of polygonal faults and mud crack patterns is that lithology may influence the rate of elastic energy release. As Corte and Higashi (1960) mention, when the transformation of elastic energy to surface energy occurs slowly, a single fracture propagates and alters the surrounding stress field. Such an altered stress field will force the later forming cracks to intersect the previous cracks at 90° (Lachenbruch, 1962), forming patterns dominated by orthogonal intersections. On the other hand, if the elastic energy is transformed to surface energy at a fast rate, multiple cracks will be simultaneously initiated on the surface to release elastic energy. In this case, shallow cracks will tend to form triple junctions since this is the form that creates the least amount of surface area. The energy transformation rate is usually determined by the amount of elastic energy stored within the material and the friction between layers. For example, fractures in sand-rich material with strong friction may only occur

when a lot of strain energy is stored; hence, the energy transformation rate will be fast. On the other hand, in less strong, clay-rich materials, elastic energy will be released once the stress overcomes the weak cohesion between materials, which keeps the stored elastic energy at a low value and a slow rate of transformation. This implies that triple junction-dominated patterns are unlikely to occur in polygonal faults generated at clay-rich sediments. Even if hexagonal pattern polygonal faults occur in sand-rich sediments, the fault length will be much shorter than in the polygonal faults in clay-rich sediments.

CONCLUSIONS

Polygonal faults are understudied and important for understanding porosity and permeability evolution during burial. The multiplicity of scales for these types of structures can have profound effects on local permeabilities with cracks or fractures dominating over host-rock permeability allowing fluids to escape preventing fluid pressure buildups or retention of fluids. Alternatively, sealed polygonal faults may allow local fluid pressure to buildup enhancing poroelastic effects that might foster local uplift.

(1) Field study suggests that layer-bounded minor displacement polygonal faults exist within the Austin Chalk Formation in North Texas. These polygonal faults are syndepositional and many are intraformational at the rock member scale. The faults have no preferred tectonic , i.e. the faults are not subparallel and thus, were likely initiated at shallow depth in the Late Cretaceous, predating the earlier Balcones faults where they are present.

(2) The direction of drainages is predominately influenced by the topography but can also reflect the underlying fault orientations within the Austin Chalk, particularly for lower order drainages close to stream headwaters. Balcones faults have the most decisive influence on drainage directions which coincidentally are crudely parallel to the regional strike and dip of the Cretaceous formations. In Central and South Texas, where the fault density is highest, the Balcones faults may also have striated fault hosted calcite veins; this could not be confirmed in Dallas County. On the other hand, polygonal faults also influence drainages in North Texas, as reflected in the first-order streams.

(3) Results from lab experiments and field observations show scale invariance over 7 orders of magnitude between the relationship of polygon area and fracture thickness. The relationship is $\log(\text{Area}) \approx 1.9 \log(\text{depth}) + 2.6$.

(4) Crack patterns are invariant with thickness but vary with lithology. In clay-rich and calcareous mud-rich materials, crack patterns are dominated by orthogonal cracks, while as the percentage of silica sand increases, the number of orthogonal intersections increases accordingly.

(5) Based on the new implication on the structure, the oxygen isotopes of veins and host rocks suggest that calcite veins were precipitated during the initiation of polygonal faults and perhaps when Balcones faults where present. Veins precipitated during the propagation of polygonal faults formed under fluid-buffered conditions with fluids that have isotopic composition similar to epicontinental seawater and at very shallow depth. Real variations in the oxygen isotopic composition of seaways isolated or distance from the well mixed open ocean account for the greatest uncertainty in burial depth estimates from the difference between unreacted host rocks and veins precipitated from formation water.

FIGURES

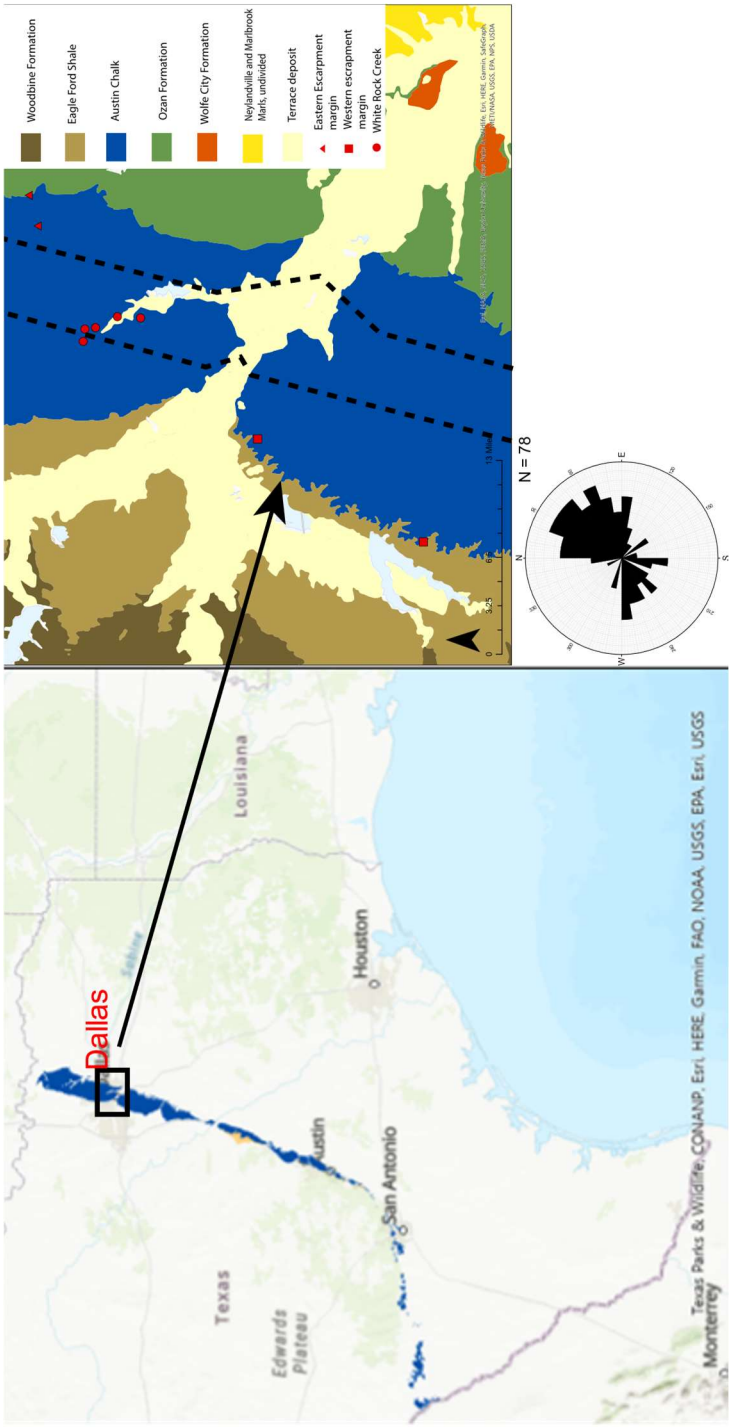

Figure 1: Austin Chalk outcrop distribution plotted on top of a regional scale map of Texas with the square showing the location of the smaller scale geologic map. The Rose diagram, below reflects the strike directions of field-measured fault planes. Locations of the outcrops are labeled with red pins. Dashed lines are the boundaries between the upper, middle, and lower members of the Austin Chalk.

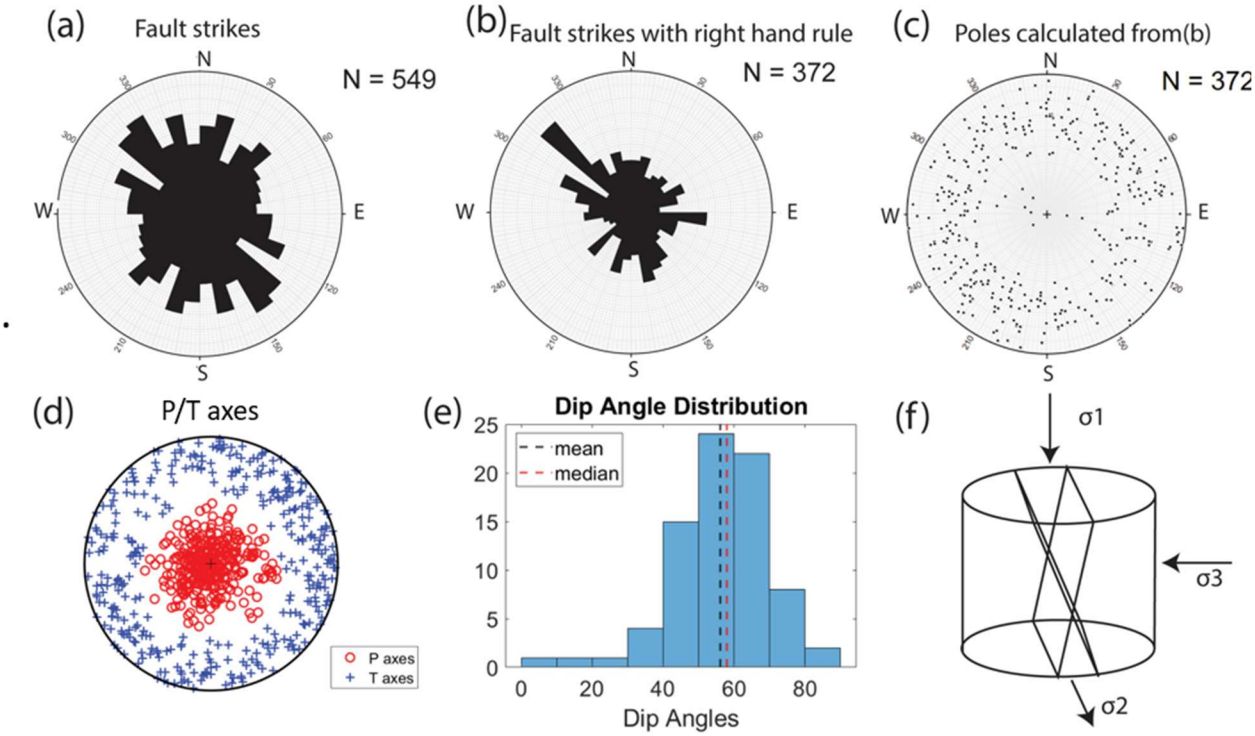

Figure 2: Rose diagram, poles, and stress inversion result of measured fault planes in Dallas and Ellis County by this and previous studies. (a) Rose diagram of all faults with strike measurements, (b) rose diagram of all faults with both strike and dip measurements from this study and previous studies. (c) calculated poles from to fault planes with strike and dip measurements. (d) P and T axes calculated from the strike and dip data in (b) using *StressInverse* (Vavryčuk, 2014). (e) Distribution of normal fault dip angles in the Austin Chalk. (f) Cylindrical stress test diagram showing of principal stress axes associated with normal fault planes

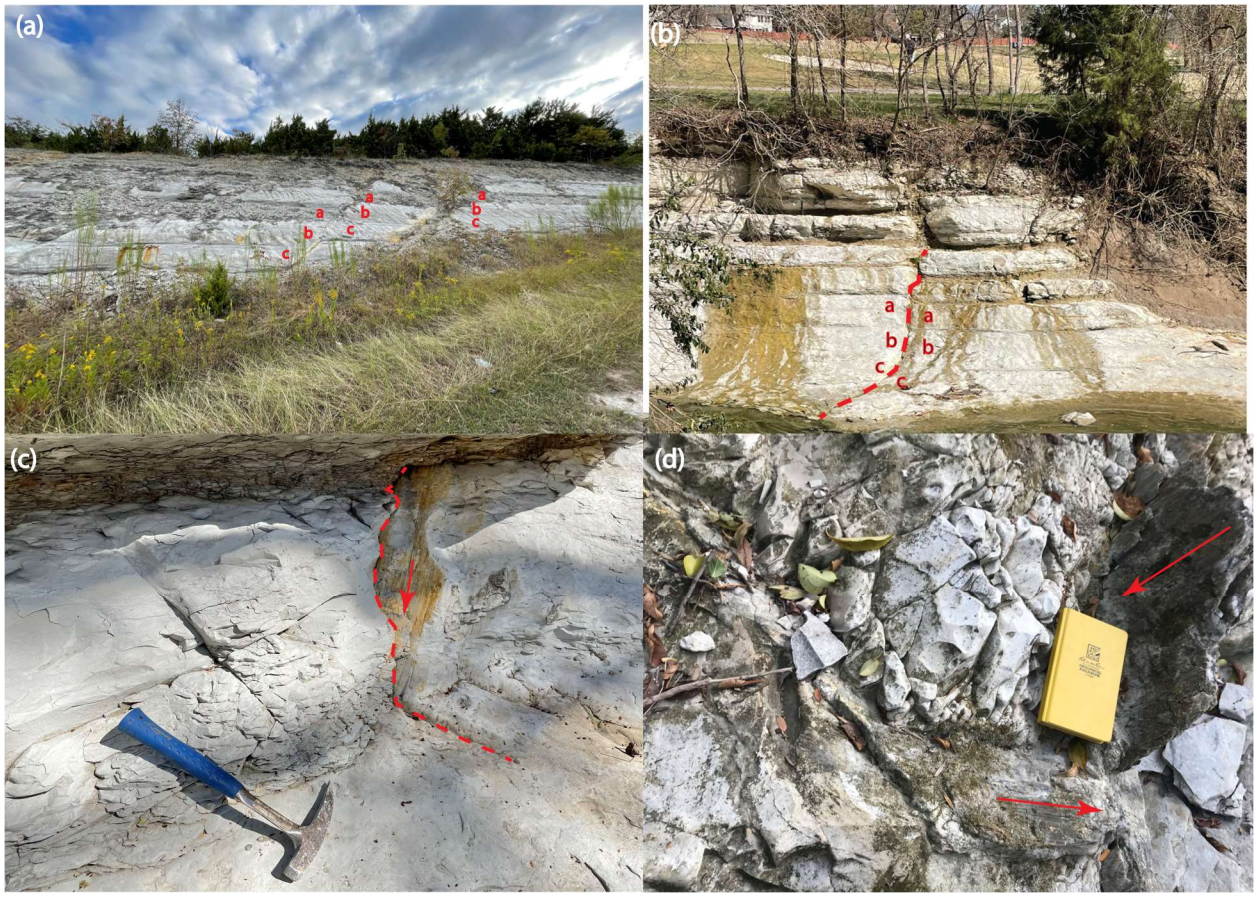

Figure 3: Field images of normal faults in Austin Chalk formation. (a) parallel normal faults in Atco member with small displacement. The dips are in the image are apparent dips. (b) Curvilinear normal fault on Hutchins unit showing the offset between layers labelled a, b and c. (c) Oblique view of normal fault that separates footwall rocks to the right and hanging wall rocks to the left of the dashed red line. The fault plane projects under the hanging-wall shale to give an apparent truncation at contact between shale and chalk which instead is the result of the oblique view with the trace of the fault buried under the grassy ledge. (d) intersection between two fault planes just below the yellow notebook. Movements are indicated by the slickensides.

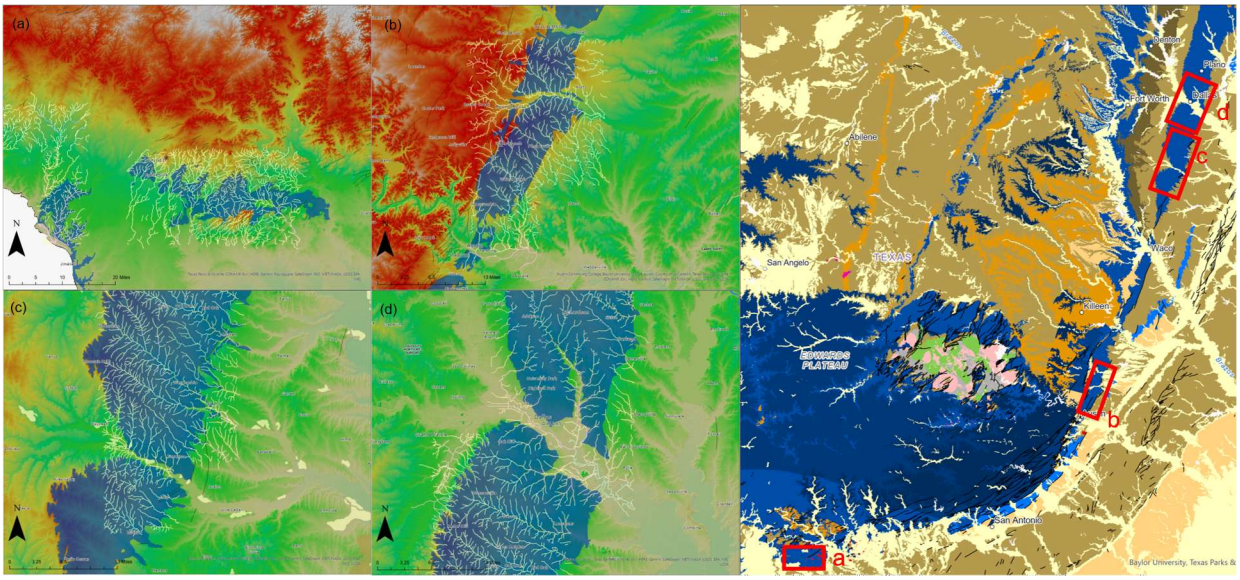

Figure 4: USGS stream data superimposed on the topographic maps of (a) South Texas west of Uvalde, (b) Central Texas near Austin, (c) Ellis County, and (d) Dallas County. The blue color reflects the distribution of the Austin Chalk formation in these regions, and the locations of these areas are labeled on the Austin Chalk outcrop belt map in the upper right corner. Red color represents high elevation, and green color represents low elevation.

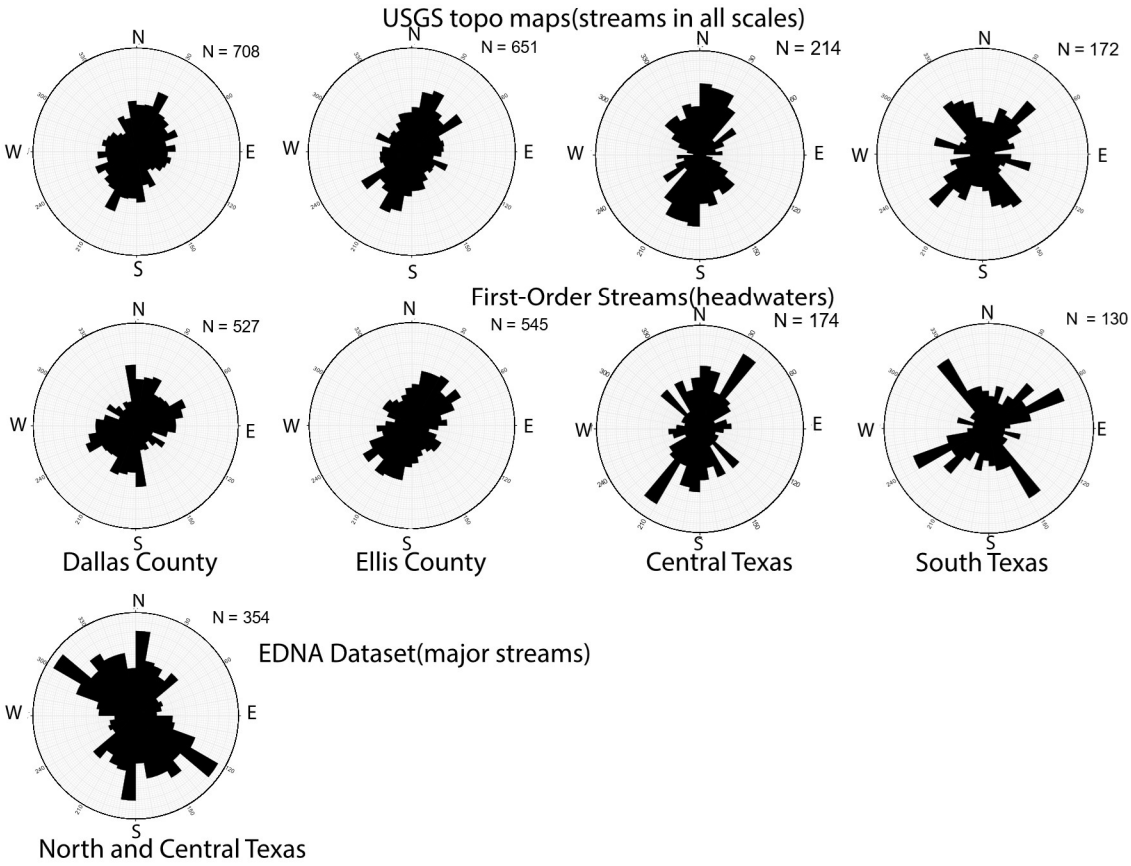

Figure 5: Rose diagrams showing the direction of streams in USGS topo maps, DEM first order streams, EDNA major streams

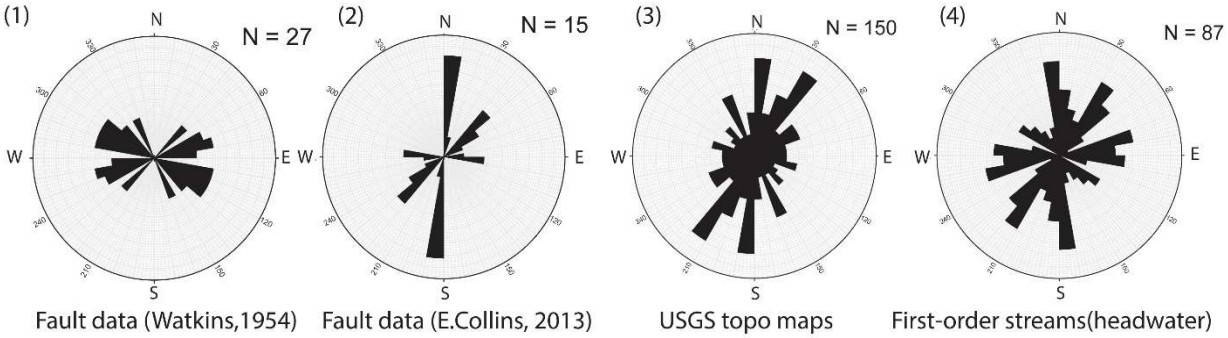

Figure 6: Comparison of drainage and fault direction within the Cedar Hill quadrangle. From left to right are (1) the direction of normal faults measured in this area by Watkins (1954), (2) the direction of normal faults measured in this area by E. Collins (2013), (3) the direction of the drainages in the USGS topo maps over the Cedar hill quadrangle, (4) Direction of the first order streams from DEM's over the Cedar hill quadrangle.

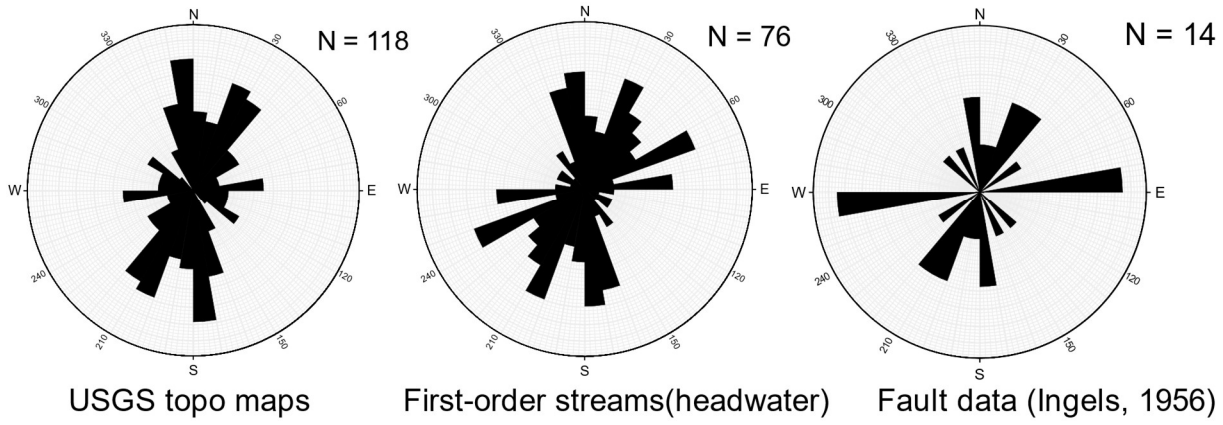

Figure 7: Rose diagrams of drainages cutting the Austin Chalk over the Lancaster quadrangle. The left rose diagram is streams in the 1:24000 USGS topo maps, the middle rose diagram is the first-order streams, and the right rose diagram contains faults measured by Ingels (1956).

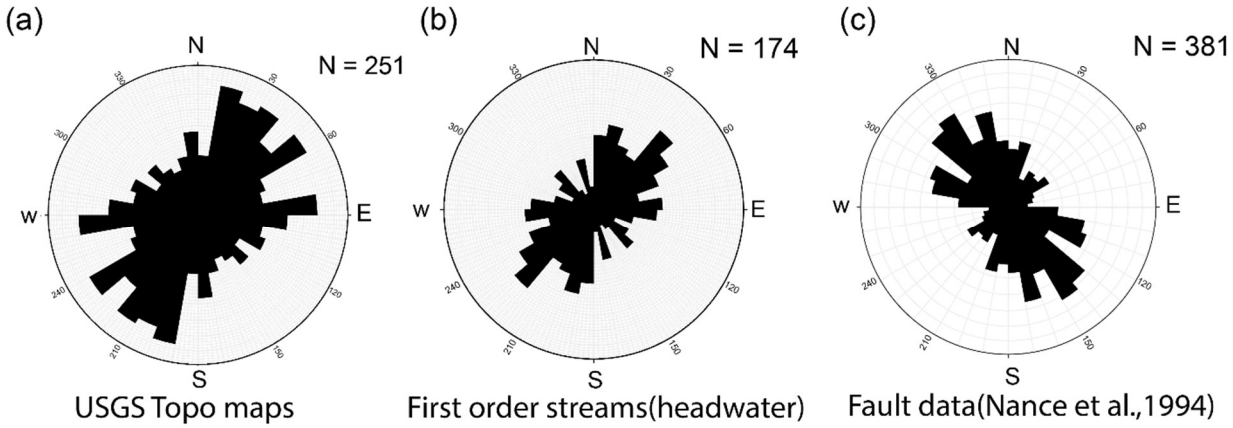

Figure 8: Drainage and fracture orientations over the Waxahachie and Midlothian quadrangle. (a) USGS topo map drainages over Midlothian and Waxahachie quadrangles (b) extracted first order streams over Midlothian and Waxahachie quadrangles (c) faults in the tunnel of superconducting super collider measured by Nance et al., 1994

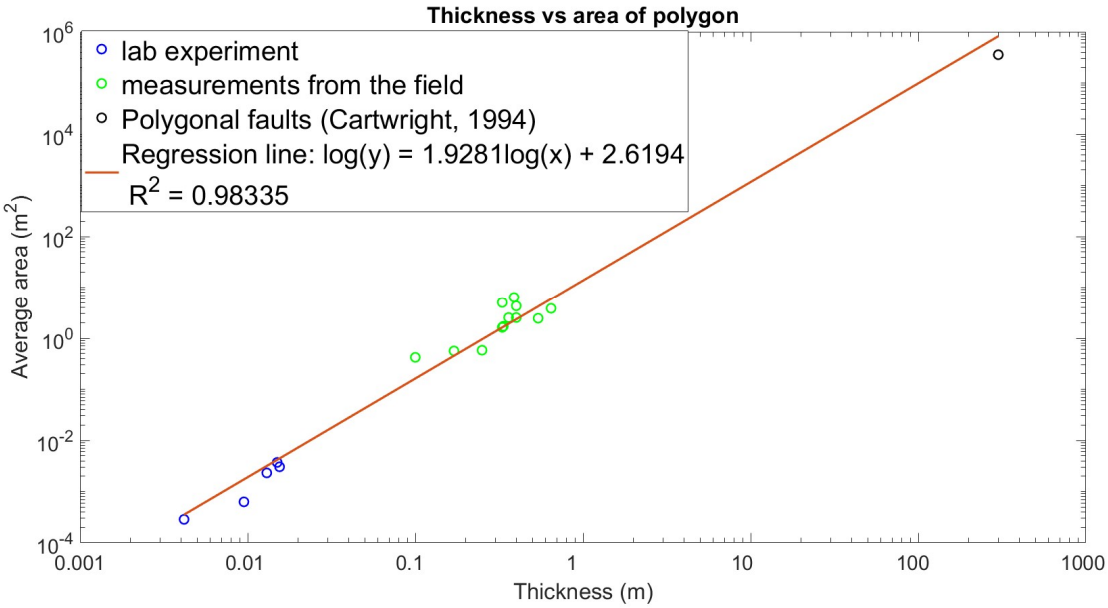

Figure 9: Log-log scale plot of thickness vs area of polygons formed in mudcracks and polygonal faults. The graph shows three sets of data, including centimeter-scale lab experiments conducted with White Rock overbank deposits, on site measurements of naturally-formed mudcracks in decimeter to meter scale on the same material, and the actual polygonal faults in the North Sea (Cartwright,1994); The regression line show well correlation between three data sets.

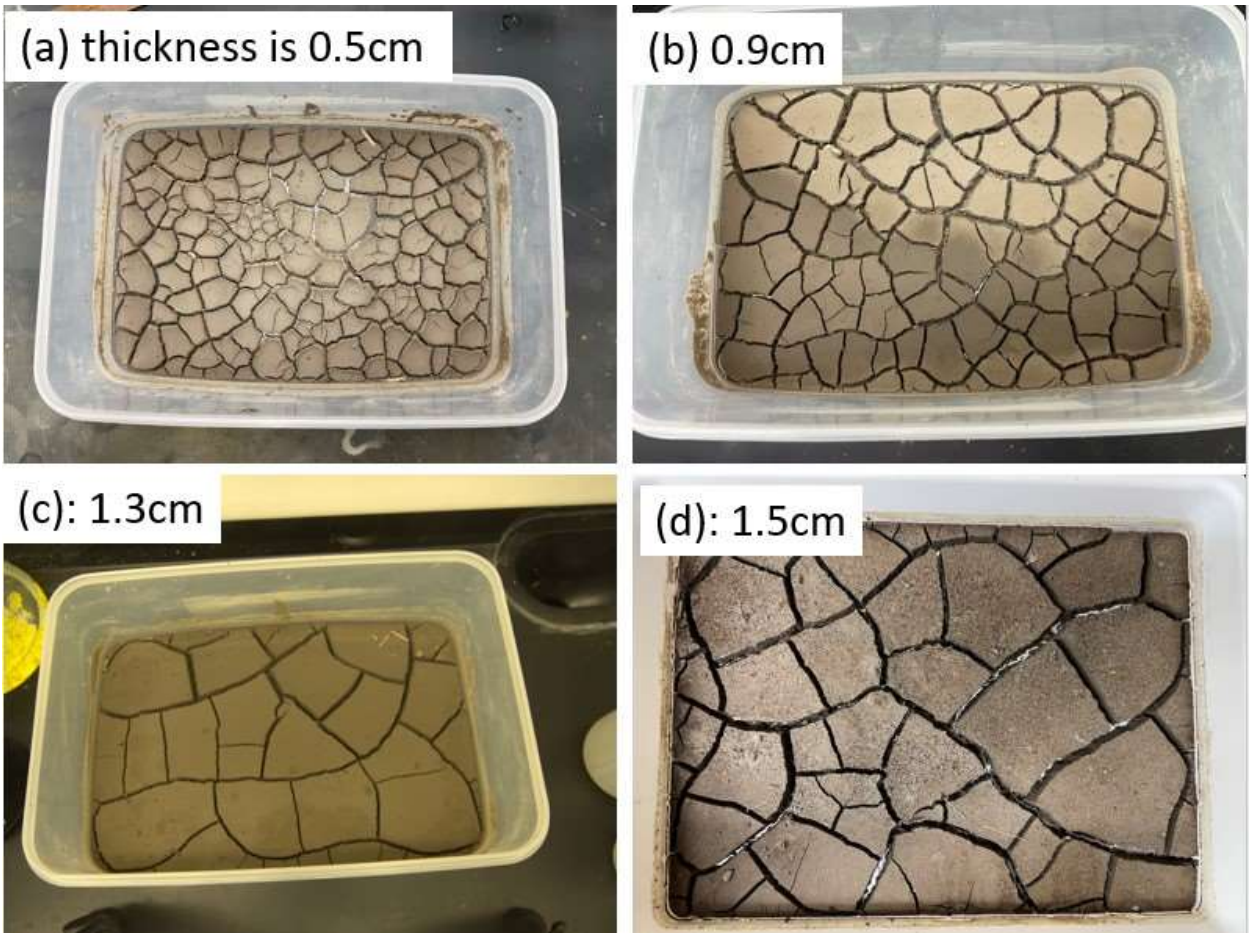

Figure 10: Crack patterns formed in White Rock Creek overbank materials with various thicknesses. The material used in these experiments is White Rock Creek over bank flood deposit. Experiments (a) to (c) are done on a tray with dimension of 27 by 20cm, while experiment (d) is done on a tray with dimension of 44.45 by 34.29cm. Resultant crack patterns are similar in that most of the intersection angles are orthogonal, and the thicknesses from (a) to (d) are 0.45cm, 0.9cm, 1.3cm, and 1.55cm, respectively.

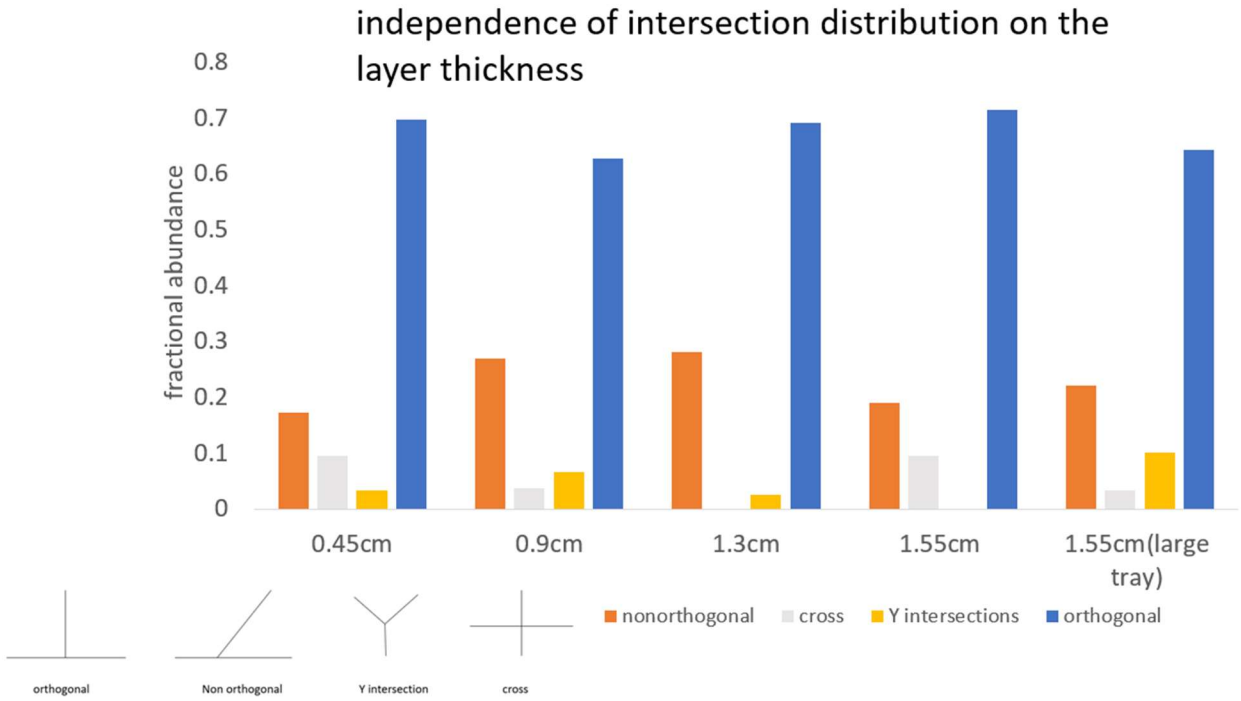

Figure 11:Fracture pattern with increasing thickness on White Rock Creek overbank materials. The intersection angles are categorized into four types, which are orthogonal, nonorthogonal, Y intersections, and cross. The graph shows that variation in layer thickness does not greatly affect the distribution of different types of intersections.

Figure 12: Crack pattern formed by inhomogeneous mixing between bentonite and Austin Chalk. The middle section has higher percentage of bentonite clay than the left and right sides, which resulted in larger polygons with wider cracks and more “orthogonal” intersections in the center than on the sides.

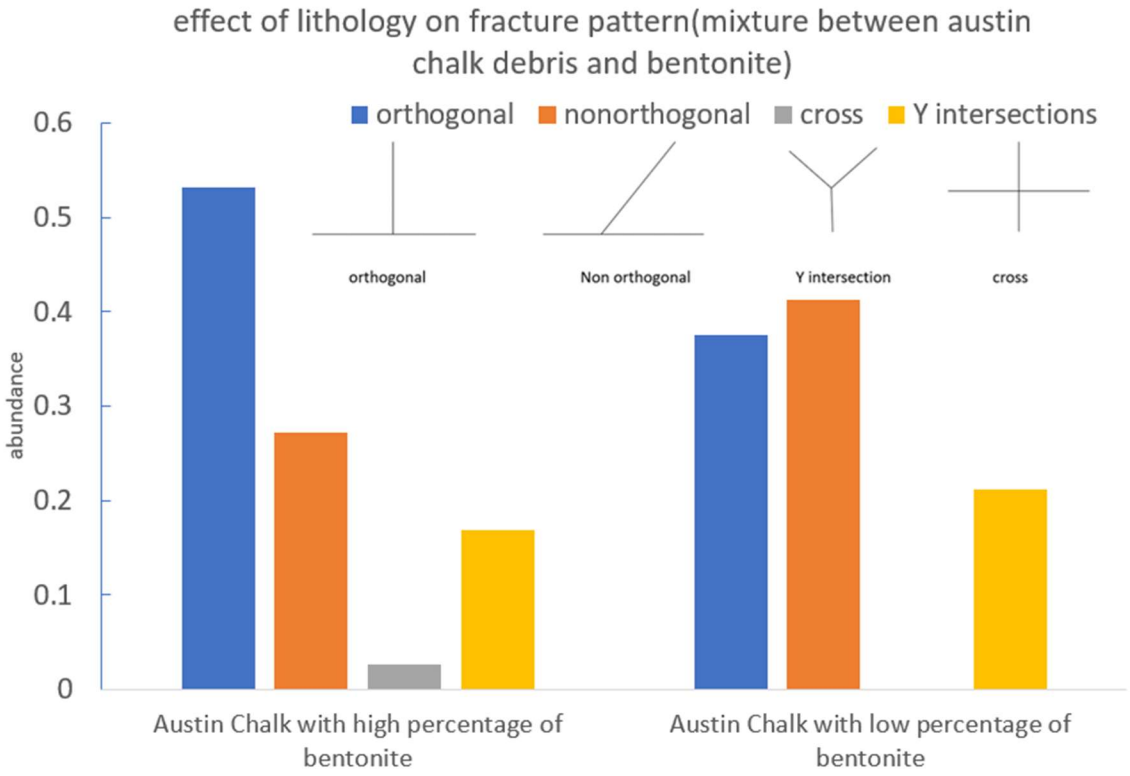

Figure 13: Fracture pattern variation as the proportion of powdered Austin Chalk and bentonite varies. In places where the percentage of bentonite is relatively high, cracks form large polygons with mostly orthogonal intersections. On the other hand, in places where the percentage of bentonite is low, cracks form small polygons and most of the intersections are nonorthogonal.

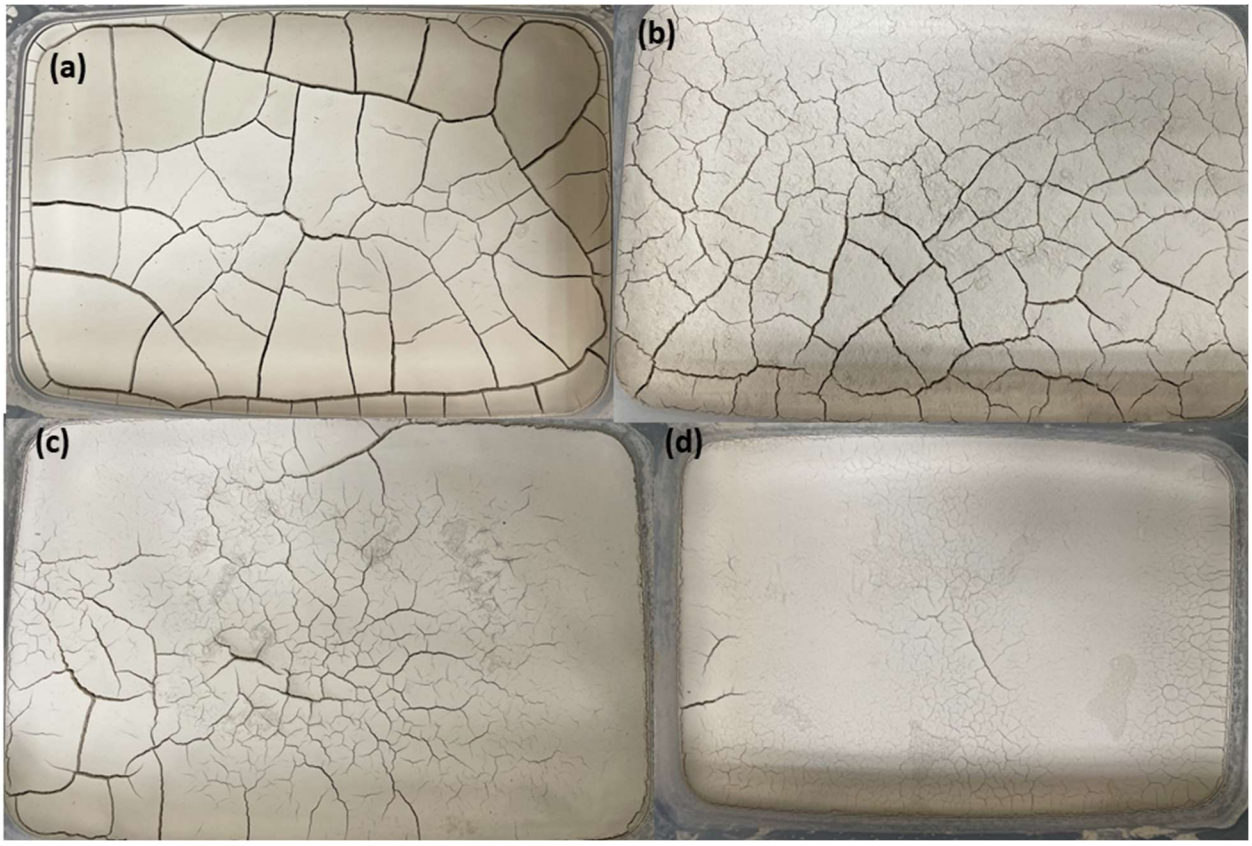

Figure 14: Photos of mudcrack patterns after fully desiccating the materials. From (a) to (d), the percentage of silica sand gradually increases from a to d from 0 to 35, 42, and 47 % from (a) to (d) respectively while the weight of the calcareous sediment in each experiment stays relatively constant. As a result, cracked polygons become smaller and the type of intersections changes from orthogonal to Y intersections.

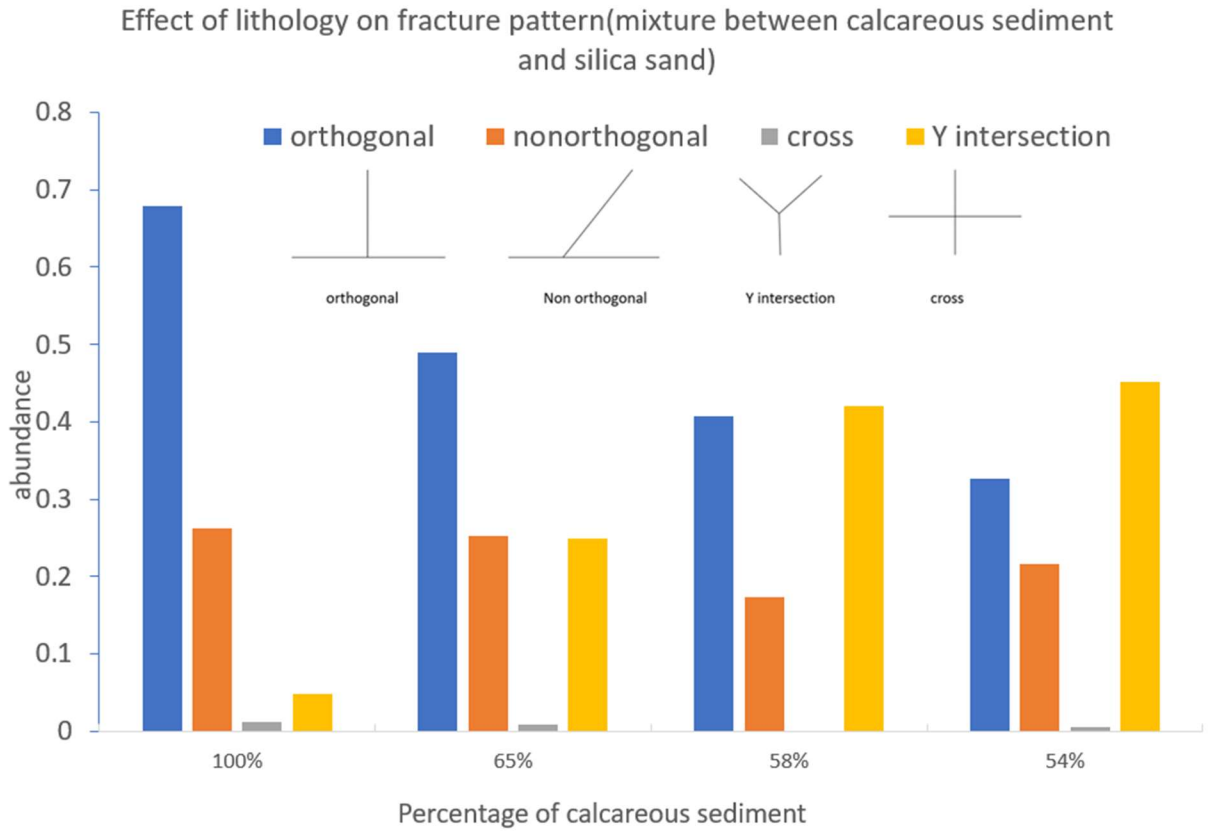

Figure 15:Fracture pattern variation in mixture of different proportions of calcareous sediment and silica sand. The intersection angles are categorized into four types, and the frequency of each type of intersection is counted. The diagram shows that as the percentage of silica sand material increases, the number of orthogonal intersections decreases.

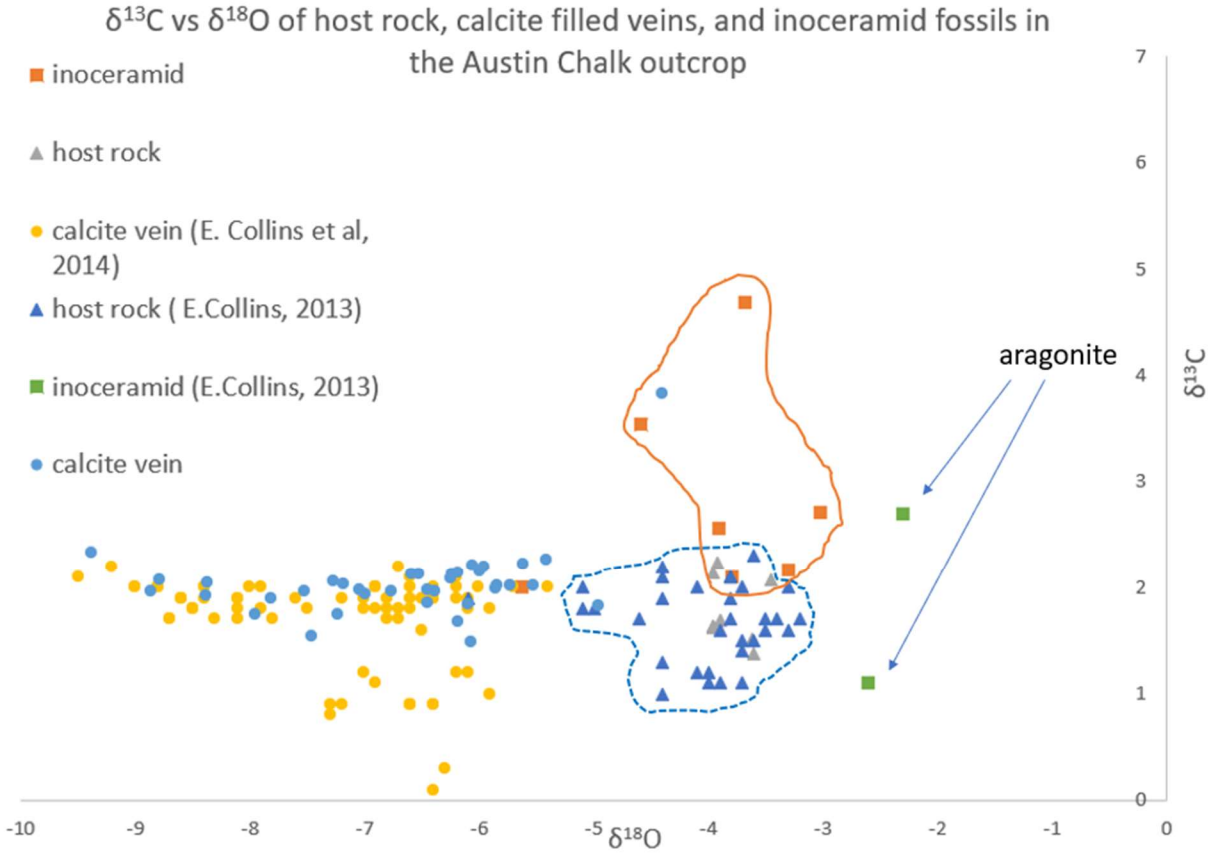

Figure 16: Oxygen and carbon isotopic composition data of calcite veins, *Inoceramid* fossils, and host-rock chalk measured in E.Collins (2013) and this study. The variance in $\delta^{18}O$ of veins relative to the chalk samples suggests that veins are not rock-buffered because the veins are systematically lower in $\delta^{18}O$ than their coexisting host rocks. Primary aragonite in the benthonic *Inocerimids* is enriched when compared with the chalk. The *Inocerimids* in the orange squares overlap with the oxygen isotope range for the chalks dominated by planktonic fossils suggesting possible diagenetic modification to calcite.

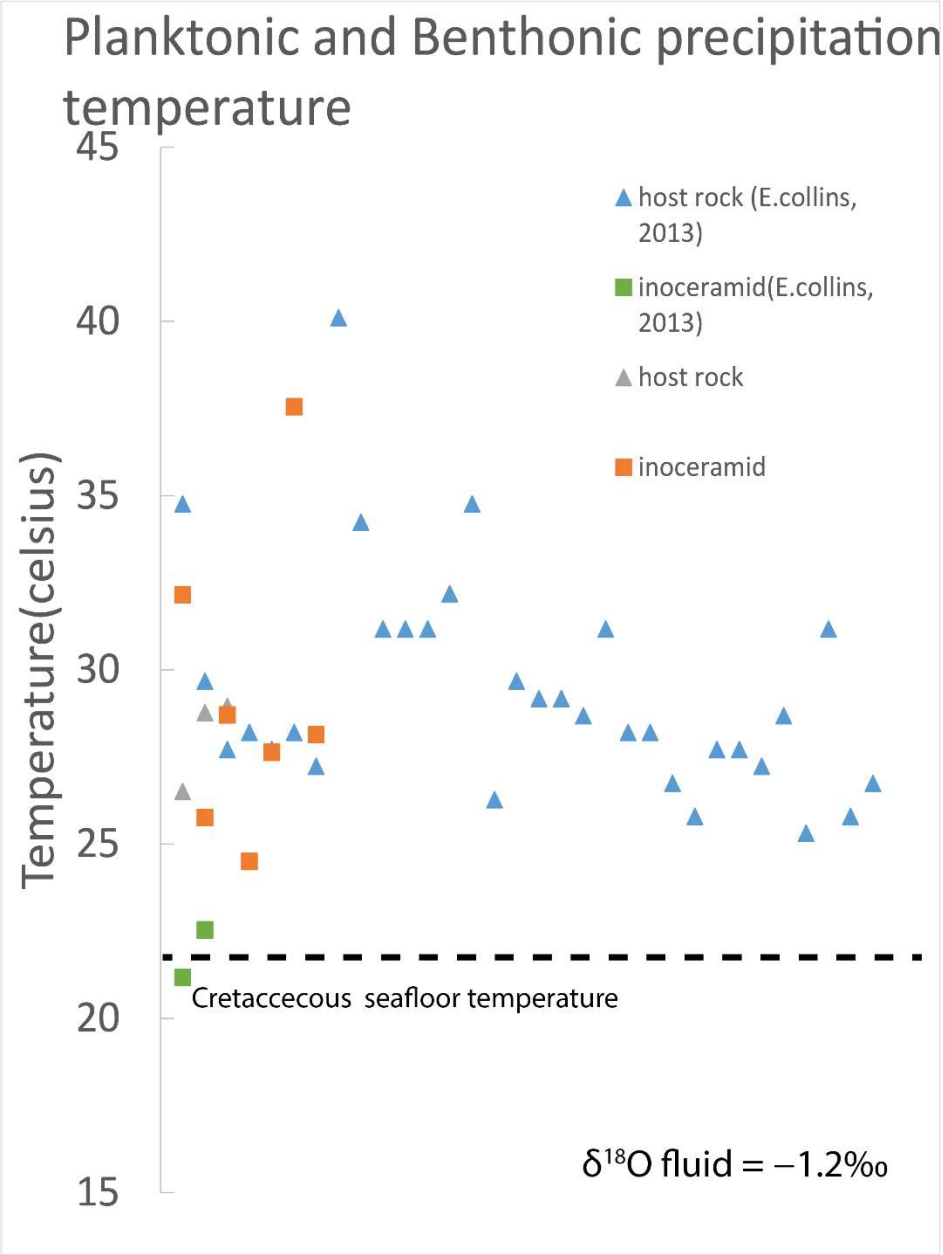

Figure 17: Calculated precipitating temperature of host rock and *Inoceramid* samples measured in this study and E. Collins (2013). These temperatures are calculated used the paleotemperature equation of O'Neil et al.(1969) corrected by Yapp (1979). The result shows that our *Inoceramid* overlaps with that of the host rock, while those collected by E.Collins were primary aragonite and show the bottom water temperature in the Cretaceous Ocean. Therefore, our *Inoceramid* samples were likely diagenetically altered.

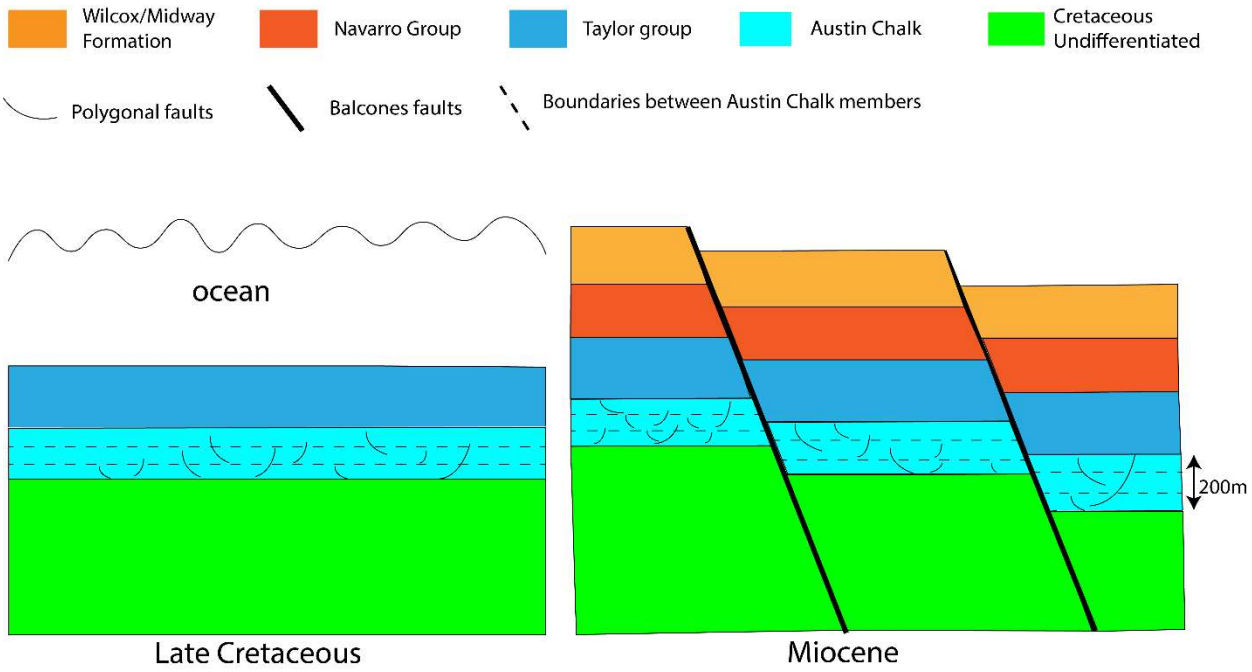

Figure 18:graph illustrating the formation of polygonal faults and Balcones faults. Balcones fault likely formed syndepositionally during late Cretaceous, while Balcones faults formed later during Miocene.

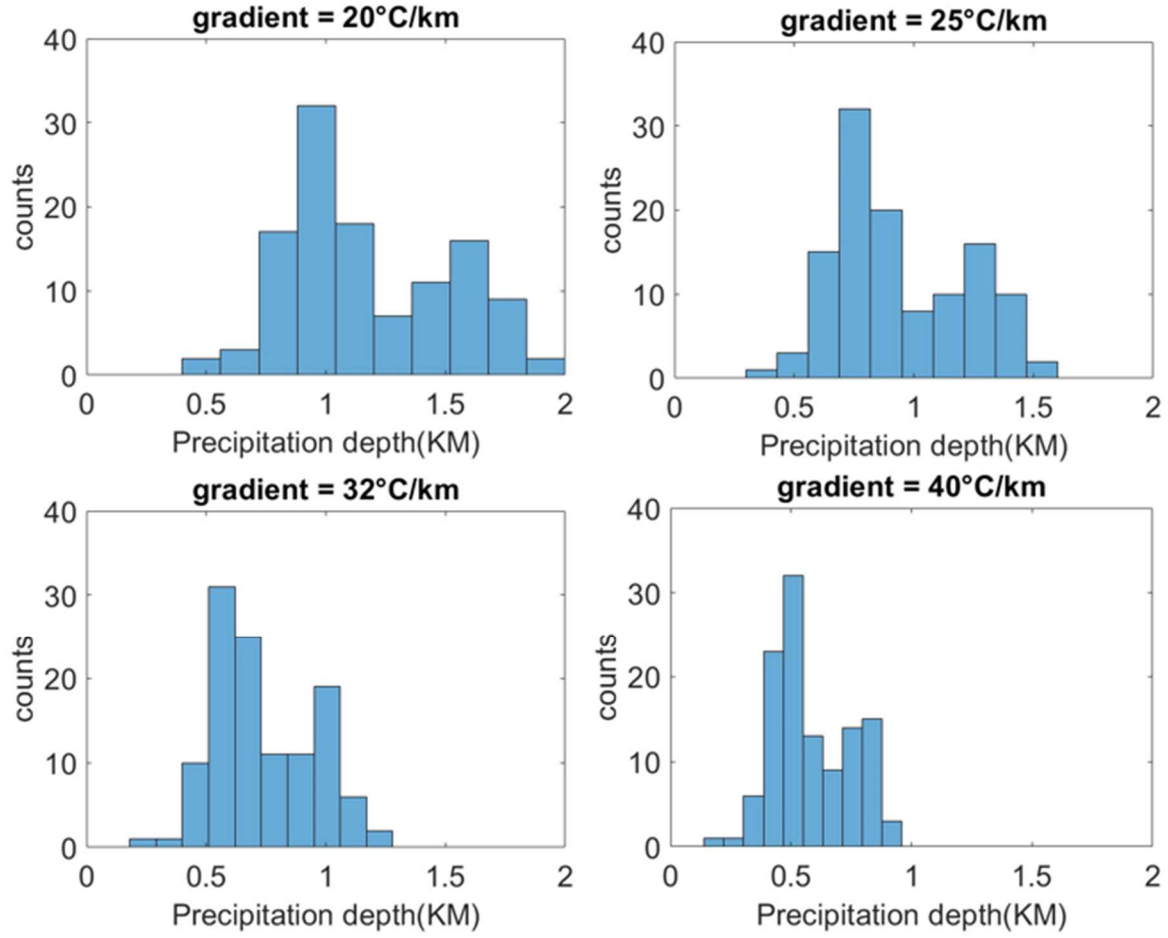

Figure 19: Calculated precipitating depth of calcite veins given different geothermal gradients. The vein precipitation temperature is calculated assuming fluid-buffered and $\delta^{18}O$ value is −1.2‰. Seafloor temperature is set to 21°C.

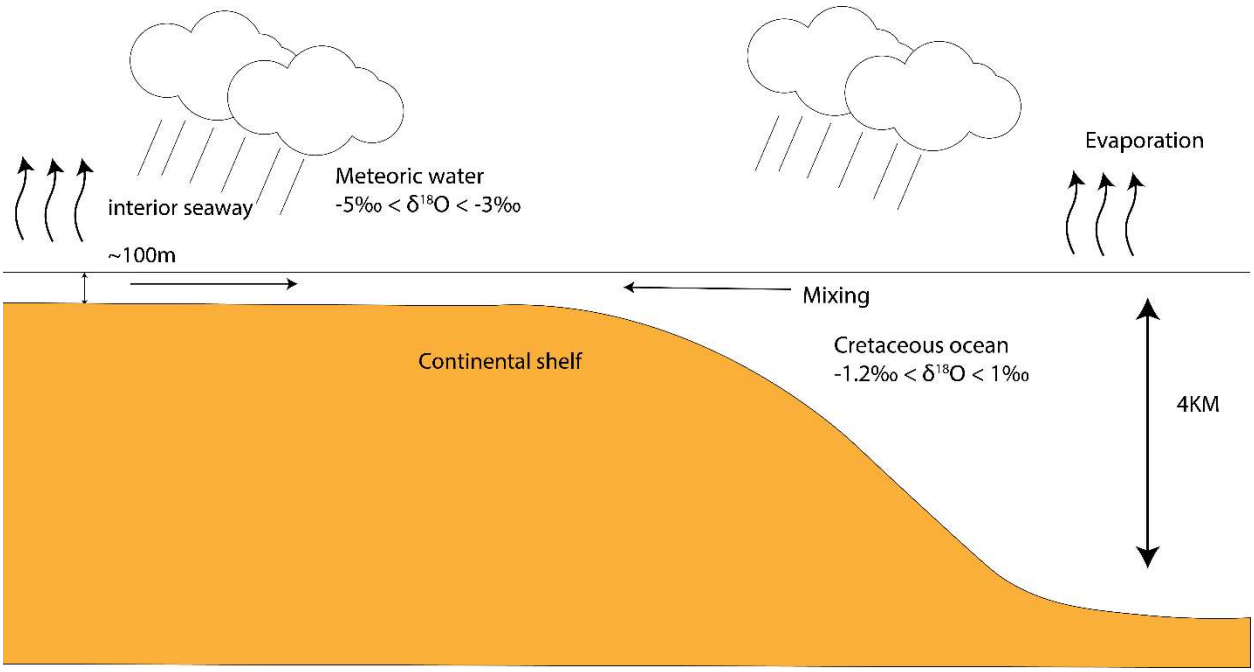

Figure 20:Illustration figure on how δ_{fluid} may varies with the meteoric water, seawater, and evaporation.

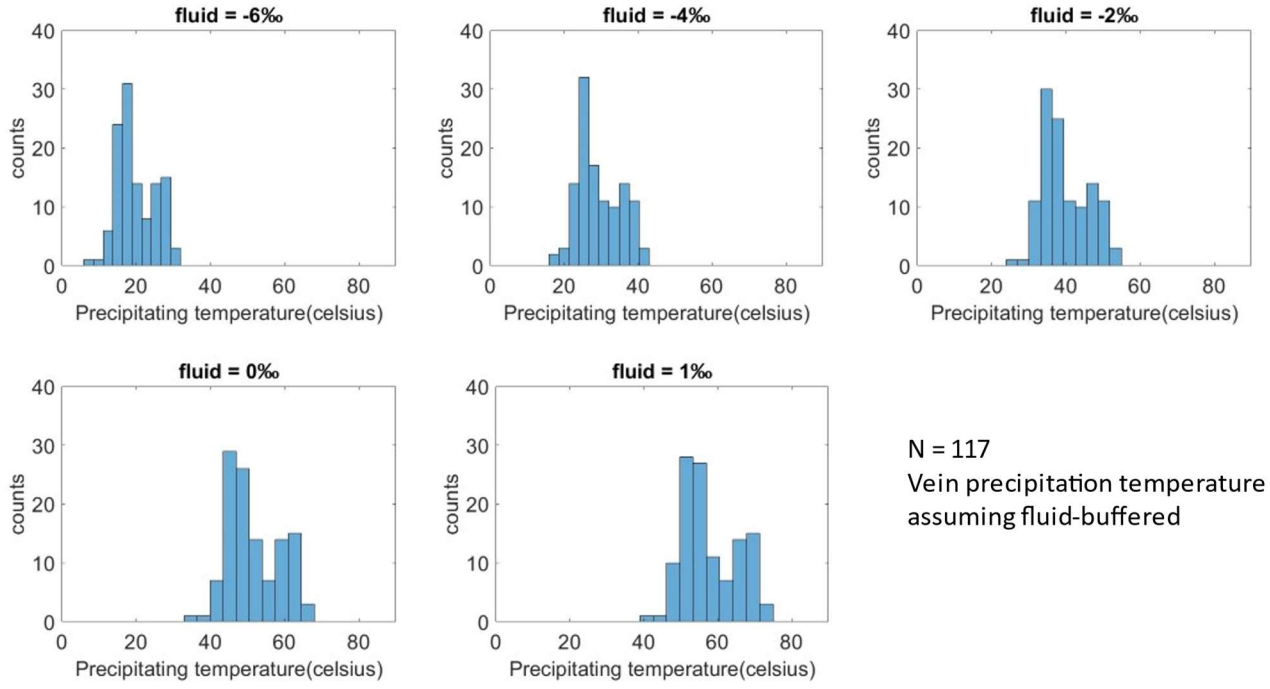

Figure 21:precipitating temperature of calcite veins based on different fluid compositions. The $\delta^{18}O$ value for seawater may vary from 1 to −1.2‰, and the meteoric water may be as depleted as −8‰.

BIBLIOGRAPHY

Allmendinger, R. (2011). *Stereonet 11*(Version 11.5.1) [Computer Software]. https://www.rickallmendinger.net/stereonet

Athy, L. F. (1930). Density, Porosity, and Compaction of Sedimentary Rocks1. *AAPG Bulletin*, *14*(1), 1–24. https://doi.org/10.1306/3D93289E-16B1-11D7-8645000102C1865D

Berner, R. A. (1980). Early Diagenesis: A Theoretical Approach. Princeton University Press. https://doi.org/10.2307/j.ctvx8b6p2

Blackwell, David, M. Richards, Z. Frone, J. Batir, A. Ruzo, R. Dingwall, and M. Williams 2011, Temperature at depth maps for the conterminous US and geothermal resource estimates, GRC Transactions, 35 .

Blakemore, E. F. Jr. (1939) "Drainage Controls in the Austin Chalk Cuesta Area of Dallas, Texas," Field and Laboratory: Vol. 7: No. 2

Cartwright, J. (2011). Diagenetically induced shear failure of fine-grained sediments and the development of polygonal fault systems. Marine and Petroleum Geology, 28(9), 1593-1610.

Cartwright, J. A. (1994). Episodic basin-wide hydrofracturing of overpressured Early Cenozoic mudrock sequences in the North Sea Basin. Marine and Petroleum Geology, 11(5), 587–607. https://doi.org/10.1016/0264-8172(94)90070-1

Cartwright, J. A., & Dewhurst, D. N. (1998). Layer-bound compaction faults in fine-grained sediments. Geological Society of America Bulletin, 110(10), 1242–1257. https://doi.org/10.1130/0016-7606(1998)110<1242:LBCFIF>2.3.CO;2

Cartwright, J. A., & Lonergan, L. (1996). Volumetric contraction during the compaction of mudrocks: A mechanism for the development of regional-scale polygonal fault systems. Basin Research, 8(2), 183-193.

Collins, E. M. (2013). Calcite-filled veins of the Austin Chalk Formation: Using a combination of geochemistry and structural geology to constrain the post-depositional history (Doctoral dissertation, Southern Methodist University).

Collins, E.M., Feguson, K.M., Gregory, R.T. , (2014). Stable isotope ratios of coexisting veins and host rocks constrain the burial history of the Austin Chalk, Goldschmidt 2014, 444

Collins, E. W., and S. D. Hovorka, 1997, Structure map of the San Antonio segment of the Edwards Aquifer and Balcones fault zone, south-central Texas: Structural framework of a major limestone aquifer: Kinney, Uvalde, Medina, Bexar, Comal, and Hays Counties: The University of Texas at Austin, Bureau of Economic Geology Miscellaneous Map 38, scale 1:250,000, 2 sheets

Collins, Edward W., Laubach, Stephen E., Vendeville, Bruno C., 1990, Faults and Fractures in the Balcones Fault Zone, Austin Region, Central Texas. Austin, Texas: Austin Geological Society, 1990. Print.

Corbett, K., Friedman, M., & Spang, J. (1987). Fracture development and mechanical stratigraphy of Austin Chalk, Texas. AAPG Bulletin, 71(1), 17-28.

Corte, A., Higashi, A. (1960). Experimental research on desiccation cracks in soil. Research Report 66.

Criss, R.E. (1999) Principles of stable isotope distribution, New York: Oxford University Press, 254 pp

Dallas Petroleum Geologists (1941). Geology of Dallas County, Southern Methodist University Press, pp. 42-53.

Davies, R. J., Ireland, M. T., & Cartwright, J. A. (2009). Differential compaction due to the irregular topology of a diagenetic reaction boundary: A new mechanism for the formation of polygonal faults. *Basin Research*, *21*(3), 354–359. https://doi.org/10.1111/j.1365-2117.2008.00389.x

Dewhurst, D. N., Cartwright, J. A., & Lonergan, L. (1999). The development of polygonal fault systems by syneresis of colloidal sediments. Marine and Petroleum Geology, 16(8), 793–810. https://doi.org/10.1016/S0264-8172(99)00035-5

Dravis, J. J. (1980). SEDIMENTOLOGY AND DIAGENESIS OF THE UPPER CRETACEOUS AUSTIN CHALK FORMATION, SOUTH TEXAS AND NORTHERN MEXICO [Thesis, Rice University]. https://scholarship.rice.edu/handle/1911/15542

Ferrill, D. A., McGinnis, R. N., Morris, A. P., Smart, K. J., Sickmann, Z. T., Bentz, M., Lehrmann, D., & Evans, M. A. (2014). Control of mechanical stratigraphy on bed-restricted jointing and normal faulting: Eagle Ford Formation, south-central Texas. AAPG Bulletin, 98(11), 2477–2506. https://doi.org/10.1306/08191414053

Ferrill, D. A., Evans, M. A., McGinnis, R. N., Morris, A. P., Smart, K. J., Wigginton, S. S., Gulliver, K. D. H., Lehrmann, D., de Zoeten, E., & Sickmann, Z. (2017). Fault zone processes in

mechanically layered mudrock and chalk. Journal of Structural Geology, 97, 118–143. https://doi.org/10.1016/j.jsg.2017.02.013

Ferrill, D. A., Evans, M. A., McGinnis, R. N., Morris, A. P., Smart, K. J., Lehrmann, D., Gulliver, K. D. H., & Sickmann, Z. (2020). Fault zone processes and fluid history in Austin Chalk, southwest Texas. *AAPG Bulletin*, *104*(2), 245–283. https://doi.org/10.1306/04241918168

Foley, L. L. (1926). Mechanics of the Balcones and Mexia Faulting. *AAPG Bulletin*, *10*(12), 1261–1269. https://doi.org/10.1306/3D932760-16B1-11D7-8645000102C1865D

Friedman, I., & O'Neil, J. R. (1977). *Compilation of stable isotope fractionation factors of geochemical interest* (Report No. 440KK; Professional Paper). USGS Publications Warehouse. https://doi.org/10.3133/pp440KK

Goulty, N. R. (2001). Polygonal fault networks in fine-grained sediments—An alternative to the syneresis mechanism. *First Break*, *19*(2), 69–73. https://doi.org/10.1046/j.1365-2397.2001.00137.x

Goulty, N. R. (2002). Mechanics of layer-bound polygonal faulting in fine-grained sediments. Journal of the Geological Society, 159(3), 239–246. https://doi.org/10.1144/0016-764901-111

Gregory, R.T. & Ferguson, K.M.., 2004, Intrastorm variation in oxygen and hydrogen isotope ratios of precipitation from Dallas TX: 2001-2003, EOS Transactions Am. Geophys,. U, 85, C51B-1039

Gray, D. R., Gregory, R. T., & Durney, D. W. (1991). Rock-buffered fluid-rock interaction in deformed quartz-rich turbidite sequences, eastern Australia. *Journal of Geophysical Research: Solid Earth*, *96*(B12), 19681–19704. https://doi.org/10.1029/91JB01639

Gregory, R.T., Criss, R.E., Taylor, H.P., Jr., (1989a) Oxygen isotope kinetics of mineral pairs in closed and open systems : applications to problems of hydrothermal alteration of igneous rocks and Precambrian iron formations, Chemical Geology, 75, 1-42.

Gregory, R.T., Douthitt, C.B. , Duddy, I.R. Rich, P.V & Rich, T.H., 1989b, Oxygen isotopic composition of carbonate concretions for the lower Cretaceous of Victoria, Australia: implications for the evolution of meteoric waters on the Australian continent in a paleopolar environment, Earth and Planet Sci. Lett. 92, 27-42

Gregory, R.T., and D.R. Gray, D.R.(1994). Oxygen isotope composition of veins and host rocks as tracers of fluid rock interaction in the crust, Mineralogical Magazine, 58, 352-353.

Gottardi, R., & Mason, S. L. (2018). Characterization of the natural fracture system of the Eagle Ford Formation (Val Verde County, Texas). AAPG Bulletin, 102(10), 1963–1984. https://doi.org/10.1306/03151817323

Hayward, C.T. (1978). Structural Evolution of the Waco Region. Baylor Geological Studies, 34.

Hamilton, E. L. (1979). Vp/Vs and Poisson's ratios in marine sediments and rocks. The Journal of the Acoustical Society of America, 66(4), 1093–1101. https://doi.org/10.1121/1.383344

Henriet, J., De Batist, M., & VERSCHUREN, M. 1991. Early fracturing of Paleogene clays, southernmost North Sea: relevance to mechanisms of primary hydrocarbon migration. Spencer, A.M. (ed.) Generation, accumulation and production of Europe's hydrocarbons. EAPG Spec. Publ. No 1, Oxford University Press.

Iddings. (1886). The columnar structure in the igneous rock on Orange Mountain, New Jersey. American Journal of Science (1880), s3-31(185), 321–331. https://doi.org/10.2475/ajs.s3-31.185.321

Lachenbruch, A. H. (1962). Mechanics of Thermal Contraction Cracks and Ice-Wedge Polygons in Permafrost. In A. H. Lachenbruch (Ed.), GSA Special Papers (Vol. 70). Geological Society of America. https://doi.org/10.1130/SPE70-p1

Lee, Y.-J., & Morse, J. W. (1999). Calcite precipitation in synthetic veins: Implications for the time and fluid volume necessary for vein filling. *Chemical Geology*, *156*(1), 151–170. https://doi.org/10.1016/S0009-2541(98)00183-1

Lee, Y.-J., Wiltschko, D. V., Grossman, E. L., Morse, J. W., & Lamb, W. M. (1997). Sequential vein growth with fault displacement: An example from the Austin Chalk Formation, Texas. *Journal of Geophysical Research: Solid Earth*, *102*(B10), 22611–22628. https://doi.org/10.1029/97JB01945

Lee, Y.-J., & Wiltschko, D. (2000). Fault controlled sequential vein dilation: Competition between slip and precipitation rates in the Austin Chalk, Texas. Journal of Structural Geology, 22, 1247–1260. https://doi.org/10.1016/S0191-8141(00)00045-6

Lonergan, L., Cartwright, J., & Jolly, R. (1998). The geometry of polygonal fault systems in Tertiary mudrocks of the North Sea. Journal of Structural Geology, 20(5), 529–548. https://doi.org/10.1016/S0191-8141(97)00113-2

McCrea, J. M. (1950). On the Isotopic Chemistry of Carbonates and a Paleotemperature Scale. *The Journal of Chemical Physics*, *18*(6), 849–857. https://doi.org/10.1063/1.1747785

Medetbekova, M. K., Hajiabadi, M. R., Brovelli, A., Christensen, H. F., & Nick, H. M. (2022). An integrated rock-mechanics tests and numerical modelling of chalk rocks: An improved integrated workflow for borehole safety. Journal of Petroleum Science and Engineering, 208, 109365. https://doi.org/10.1016/j.petrol.2021.109365

Meyer, K. W., Petersen, S. V., Lohmann, K. C., & Winkelstern, I. Z. (2018). Climate of the Late Cretaceous North American Gulf and Atlantic Coasts. *Cretaceous Research*, *89*, 160–173. https://doi.org/10.1016/j.cretres.2018.03.017

Murray, G.E. (1961). Geology of the Atlantic and Gulf Coastal Province of North America.

Nance, H S, Laubach, S E, & Dutton, A R. (1994). Fault and joint measurements in Austin Chalk, Superconducting Super Collider Site, Texas. United States.

Nathenson, M., & Guffanti, M. (1988). Geothermal gradients in the conterminous United States. *Journal of Geophysical Research*, *93*(B6), 6437. https://doi.org/10.1029/JB093iB06p06437

O'Neil, J. R., Clayton, R. N., & Mayeda, T. K. (1969). Oxygen Isotope Fractionation in Divalent Metal Carbonates. The Journal of Chemical Physics, 51(12), 5547–5558. https://doi.org/10.1063/1.1671982

Ogiesoba, O. C., Klokov, A., & Hernandez, R. (2015). Diffraction imaging of polygonal faults within a submarine volcanic terrain, Maverick Basin, south Texas. Interpretation, 3(1), SF81–SF99. https://doi.org/10.1190/INT-2014-0105.1

Pessagno, E. A., Jr., 1969, Upper Cretaceous stratigraphy of the western Gulf Coast area of Mexico, Texas, and Arkansas: GSA Memoir 111,139 p.

Raney et al., 1987, Geological Review of proposed Dallas-Fort Worth area site for the super conducting super collider

Reaser, D. F., & Collins, E. W. (1988). Style of Faults and Associated Fractures in Austin Chalk, Northern Extension of the Balcones Fault Zone, Central Texas. GULF COAST ASSOCIATION OF GEOLOGICAL SOCIETIES, 10.

Richards, I. J., Connelly, J. B., Gregory, R. T., & Gray, D. R. (2002). The importance of diffusion, advection, and host-rock lithology on vein formation: A stable isotope study from the Paleozoic Ouachita orogenic belt, Arkansas and Oklahoma. *GSA Bulletin*, *114*(11), 1343–1355. https://doi.org/10.1130/0016-7606(2002)114<1343:TIODAA>2.0.CO;2

Shin, H., Santamarina, J. C., & Cartwright, J. A. (2008). Contraction-driven shear failure in compacting uncemented sediments. *Geology*, *36*(12), 931–934. https://doi.org/10.1130/G24951A.1

Shuler, E. W., 1918, The Geology of Dallas County: University of Texas, Austin, Bureau of Economic Geology and Technology, Bulletin 1818, 54 p.

STRAHLER, A. N. (1952). DYNAMIC BASIS OF GEOMORPHOLOGY. *GSA Bulletin*, *63*(9), 923–938. https://doi.org/10.1130/0016-7606(1952)63[923:DBOG]2.0.CO;2

Taylor, H. P. (1968). The oxygen isotope geochemistry of igneous rocks. *Contributions to Mineralogy and Petrology*, *19*(1), 1–71. https://doi.org/10.1007/BF00371729

Tewksbury, B. J., Hogan, J. P., Kattenhorn, S. A., Mehrtens, C. J., & Tarabees, E. A. (2014). Polygonal faults in chalk: Insights from extensive exposures of the Khoman Formation, Western Desert, Egypt. Geology, 42(6), 479–482. https://doi.org/10.1130/G35362.1

The Earth Technology Corporation, 1989, Bedrock Geology of the Superconducting Super Collider Site: The Earth Technology Corporation, Report SSC-GR No.65

Vavryčuk, V. (2014). Iterative joint inversion for stress and fault orientations from focal mechanisms. Geophysical Journal International, 199(1), 69–77. https://doi.org/10.1093/gji/ggu224

Watkins, Jackie L., 1954, Geology of the Cedar Hill Quadrangle, Dallas and Ellis Counties, Texas. SMU Scholar.

Watterson, J., Walsh, J., Nicol, A., Nell, P. A. R., & Bretan, P. G. (2000). Geometry and origin of a polygonal fault system. Journal of the Geological Society, 157(1), 151–162. https://doi.org/10.1144/jgs.157.1.151

Weeks, A. W. (1945). Balcones, Luling, and Mexia Fault Zones in Texas. *AAPG Bulletin*, *29*. https://doi.org/10.1306/3D9337B0-16B1-11D7-8645000102C1865D

Williams, R., & Robinson, D. (1989). Origin and distribution of polygonal cracking of rock surfaces. Geografiska Annaler: Series A, Physical Geography, 71(3-4), 145-159.

Xia, Y., Yang, J., Chen, Y., Lu, S., Wang, M., Deng, S., Yao, Z., & Lu, M. (2022). A Review of the Global Polygonal Faults: Are They Playing a Big Role in Fluid Migration? Frontiers in Earth Science, 9. https://www.frontiersin.org/articles/10.3389/feart.2021.786915

Yapp, C. J. (1979). Oxygen and carbon isotope measurements of land snail shell carbonate. Geochimica et Cosmochimica Acta, 43(4), 629–635. https://doi.org/10.1016/0016-7037(79)90170-4

Zoback, M. L., & Zoback, M. D. (1989). Tectonic stress field of the continental United States. Geophysical framework of the continental United States, 172, 523-539.

APPENDIX A

Field measured fault plane data

Strike	dip	Location
216	51 NW	ANDERSON BONNER PARK
45	55 SE	ANDERSON BONNER PARK
67	64 SE	ANDERSON BONNER PARK
57	61 SE	ANDERSON BONNER PARK
83	41 N	ANDERSON BONNER PARK
68	63 NW	ANDERSON BONNER PARK
65	75 NW	ANDERSON BONNER PARK
55	68 SE	ANDERSON BONNER PARK
80	50 SE	ANDERSON BONNER PARK
80	57 SE	ANDERSON BONNER PARK
55	64 NW	ANDERSON BONNER PARK
82	61 N	ANDERSON BONNER PARK
48	54 NW	ANDERSON BONNER PARK
79	60 N	ANDERSON BONNER PARK
79	68 N	ANDERSON BONNER PARK
85	61 N	HAMILTON PARK
31	55 SE	HAMILTON PARK
14	61 W	HAMILTON PARK
44	59 SE	HAMILTON PARK
64	54 SE	HAMILTON PARK
71	61 SE	HAMILTON PARK
40	58 SE	HAMILTON PARK
12	46 NW	HAMILTON PARK
17	13 SE	HAMILTON PARK
22	78 SE	HAMILTON PARK
36	44 SE	HAMILTON PARK
5	9 E	HAMILTON PARK
63	44 SE	HAMILTON PARK
33	54 NW	HAMILTON PARK
28	41 SE	HAMILTON PARK
90	59 S	HAMILTON PARK
90	68 S	HAMILTON PARK

0	36 W	HAMILTON PARK
23	26 SE	HAMILTON PARK
34	77 SE	HAMILTON PARK
72	36 SE	HAMILTON PARK
7	49 W	HAMILTON PARK
81	59 N	HAMILTON PARK
53	63 SE	HAMILTON PARK
30	69 SE	HAMILTON PARK
18	49 SE	HAMILTON PARK
50	42 NW	HAMILTON PARK
65	58 SE	HAMILTON PARK
30	65 SE	HAMILTON PARK
5	41 E	HAMILTON PARK
56	66 SE	HARRY S MOSS PARK
11	70 E	HARRY S MOSS PARK
40	49 SE	HARRY S MOSS PARK
255	55 N	HARRY S MOSS PARK
70	54 SE	HARRY S MOSS PARK
75	49 SE	HARRY S MOSS PARK
65	60 SE	HARRY S MOSS PARK
85	81 S	HARRY S MOSS PARK
227	57 NW	FOREST LN
93	35 S	FOREST LN
171	72 E	FOREST LN
21	64 SE	SPRING CREEK NATURAL AREA
186	57 W	MANSFIELD ROAD
150	41 NE	MANSFIELD ROAD
7	67 E	ROCK QUARRY ROAD
358	73 E	ROCK QUARRY ROAD
12	58 SE	ROCK QUARRY ROAD
140	68 SW	ROCK QUARRY ROAD
49	78 SE	ROCK QUARRY ROAD
92	59 S	ROCK QUARRY ROAD
141	63 WSW	ROCK QUARRY ROAD
21	62 ESE	ROCK QUARRY ROAD
169	58 WSW	ROCK QUARRY ROAD
171	80 W	ROCK QUARRY ROAD
283	79 NNE	ROWLETT CREEK
112	53 SSW	ROWLETT CREEK
104	53 SSW	ROWLETT CREEK
280	49 N	ROWLETT CREEK
102	47 SW	ROWLETT CREEK
7	59 E	ROWLETT CREEK

241	43 NNW	ROWLETT CREEK
121	54 SSW	ROWLETT CREEK
226	38 NW	ROWLETT CREEK

Stable isotope data (Mass Spectrometer Output)

Sample name	Weight	Wt.% carb.	d13C	+/-	d18O(PDB)	+/-	location
1	22.89	101.8	2.040	0.009	-8.365	0.023	Anderson Bonner Park
1B(host rock)	12.32	86.5	2.075	0.029	-3.450	0.046	Anderson Bonner Park
2A	22.39	89.3	1.967	0.015	-7.523	0.026	Anderson Bonner Park
3(*Inoceramid*)	11.70	94.6	3.546	0.041	-4.594	0.051	Anderson Bonner Park
4	28.04	89.1	2.269	0.031	-5.416	0.048	Anderson Bonner Park
5(Inoceramid)	22.65	91.1	2.167	0.013	-3.294	0.027	Anderson Bonner Park
6(Inoceramid)	28.56	79.9	2.558	0.010	-3.903	0.036	Anderson Bonner Park
8(Inoceramid)	21.64	87.6	2.709	0.025	-3.022	0.033	Anderson Bonner Park
9B	12.28	93.4	2.080	0.022	-6.243	0.025	Anderson Bonner Park
9C	31.40	94.7	2.189	0.015	-5.958	0.020	Anderson Bonner Park
10A(host rock)	23.44	68.7	2.237	0.022	-3.918	0.041	Anderson Bonner Park
11	11.86	87.5	1.542	0.016	-7.463	0.018	Anderson Bonner Park
12	11.42	96.4	1.898	0.014	-7.814	0.039	Anderson Bonner Park
13	22.28	94.4	3.823	0.017	-4.396	0.028	Anderson Bonner Park
16(Inoceramid)	22.79	96.4	4.686	0.034	-3.685	0.034	Anderson Bonner Park
17	13.27	92.1	2.067	0.017	-8.787	0.023	Hamilton Park
17B(host rock)	14.54	85.7	2.146	0.021	-3.953	0.041	Hamilton Park
18	13.53	95.1	2.121	0.018	-6.589	0.023	Hamilton Park
19	16.15	90.1	1.488	0.011	-6.073	0.031	Hamilton Park
20A	25.01	89.4	1.671	0.029	-6.179	0.050	Hamilton Park
21	23.66	83.8	1.848	0.031	-6.443	0.063	Hamilton Park
22	13.90	97.1	1.967	0.010	-8.864	0.031	Hamilton Park
23	16.57	91.6	2.023	0.017	-5.733	0.015	Hamilton Park

24	12.49	94.2	1.958	0.025	-6.759	0.048	Hamilton Park
25	19.85	94.0	1.916	0.014	-8.388	0.018	Hamilton Park
26 (black)	24.56	91.1	2.130	0.015	-6.232	0.034	Hamilton Park
26 (blue)	20.87	91.1	1.967	0.029	-6.386	0.039	Hamilton Park
26B	15.88	93.4	2.013	0.012	-5.835	0.017	Hamilton Park
28	12.65	98.0	2.146	0.026	-6.182	0.031	Hamilton Park
29	12.18	100.4	2.027	0.026	-7.179	0.056	Hamilton Park
30	14.81	99.4	1.972	0.014	-7.041	0.037	Hamilton Park
31	12.26	96.4	1.935	0.023	-6.988	0.021	Hamilton Park
32	24.37	96.1	2.159	0.020	-5.995	0.026	Hamilton Park
33	10.28	94.6	2.203	0.029	-6.051	0.018	Hamilton Park
35	25.25	90.4	2.017	0.017	-5.525	0.055	Hamilton Park
36	12.06	95.6	2.228	0.017	-5.609	0.029	Hamilton Park
37	14.70	99.7	2.325	0.029	-9.387	0.058	Hamilton Park
39	13.55	86.4	1.743	0.015	-7.229	0.025	Hamilton Park
40	14.18	101.0	1.744	0.022	-7.956	0.024	Hamilton Park
45	19.10	92.2	1.973	0.019	-6.446	0.017	Hamilton Park
46 Inoceramid	13.86	89.5	2.010	0.017	-5.628	0.045	Harry S Moss Park
47	12.00	91.3	1.826	0.018	-4.952	0.019	Harry S Moss Park
48	12.04	88.5	1.837	0.027	-6.093	0.034	Harry S Moss Park
49	27.02	93.5	2.056	0.026	-7.269	0.040	Harry S Moss Park
50	11.07	94.7	1.990	0.012	-5.858	0.039	Harry S Moss Park
51	13.40	95.1	2.130	0.007	-6.519	0.041	Harry S Moss Park
52(Inoceramid)	14.59	60.9	2.098	0.015	-3.790	0.033	Harry S Moss Park
040 80(vein)	6.98	84.0	1.570	0.020	-5.890	0.017	Rock Quarry Road
1(host rock)	12.06	85.2	1.620	0.011	-3.900	0.030	Rock Quarry Road
080 70(host rock)	14.42	83.7	1.630	0.013	-3.600	0.039	Rock Quarry Road
040 80(host rock)	10.15	90.4	1.690	0.009	-3.610	0.036	Rock Quarry Road
2(host rock)	9.03	83.6	1.380	0.030	-4.040	0.029	Rock Quarry Road
3(host rock)	11.21	81.8	1.510	0.015	-4.020	0.029	Rock Quarry Road

APPENDIX B

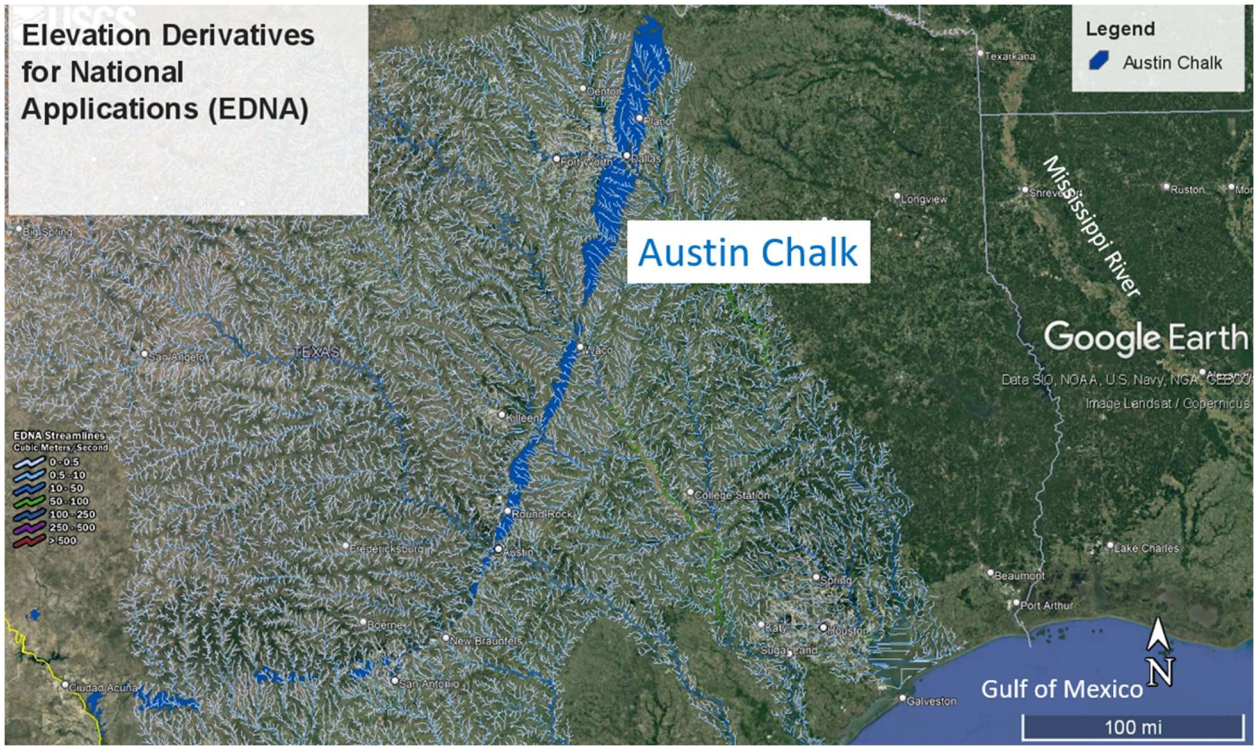

A section of EDNA drainage dataset overlying the Austin Chalk formation. Notice that most of the streams in this dataset flows in downdip direction over the Austin Chalk escarpment.

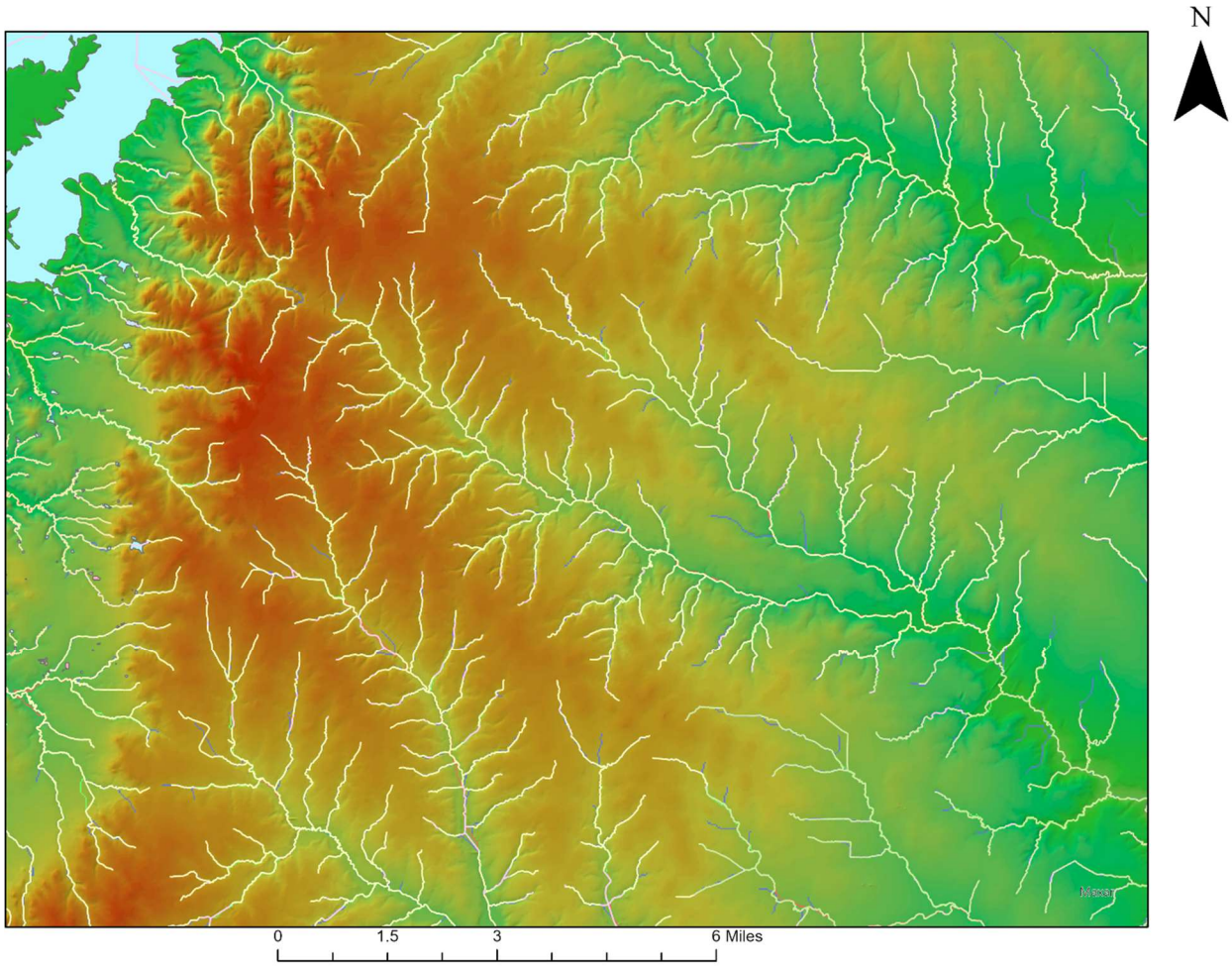

An example of USGS topo map drainage data, notice how the dataset covers most of the visible streams.

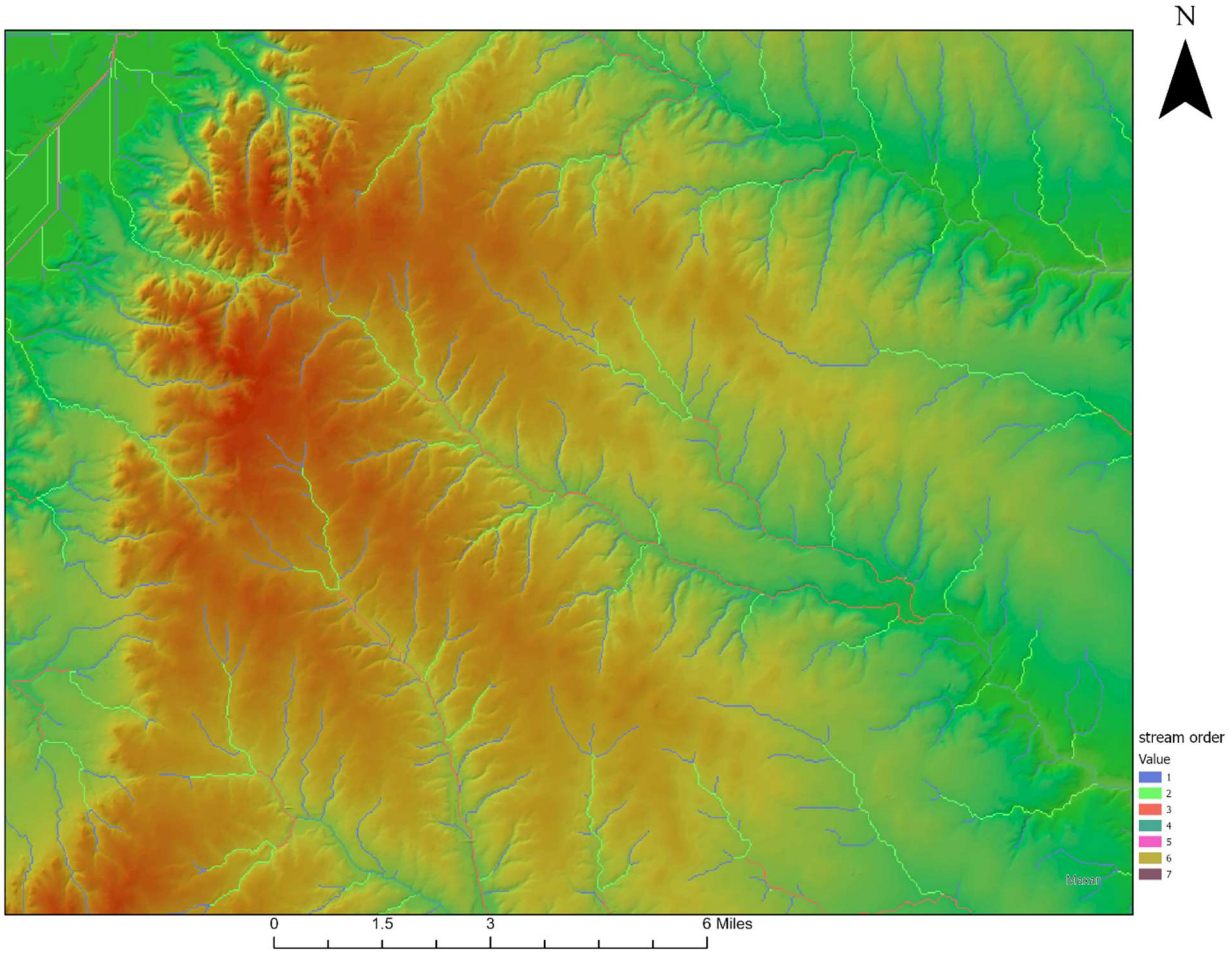

An example of drainage data separated based on the stream order. Blue color streams in this case represents first order streams (i.e. headwaters).

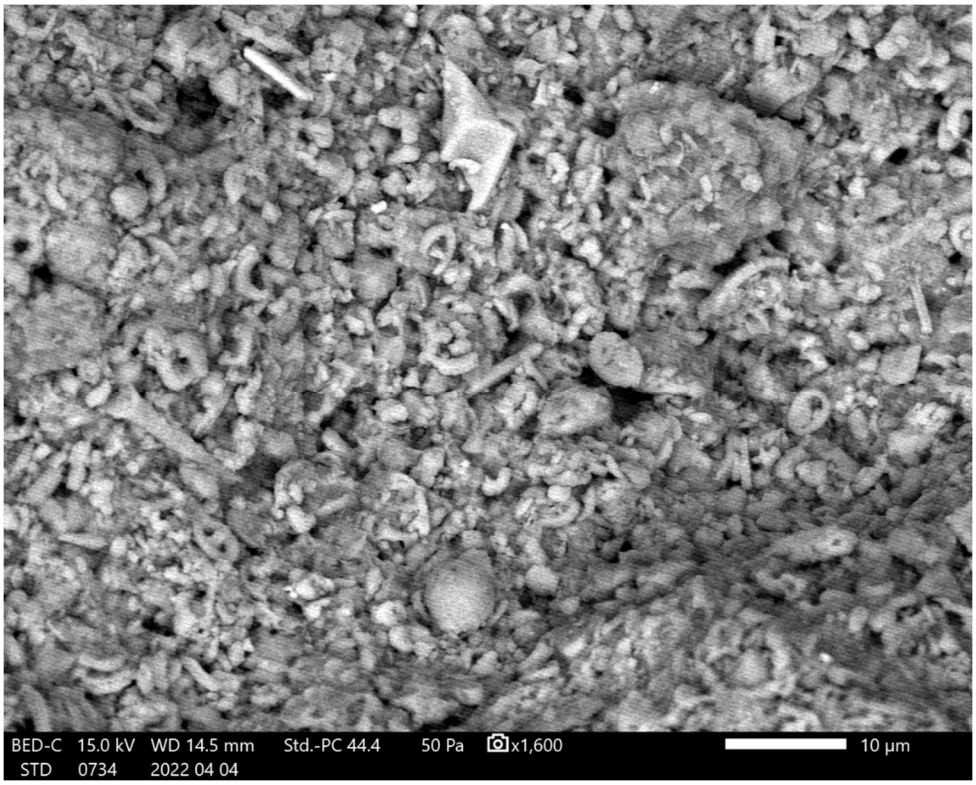

SEM image of Austin Chalk sample, the image shows that chalk is mostly composed of skeletal particles.

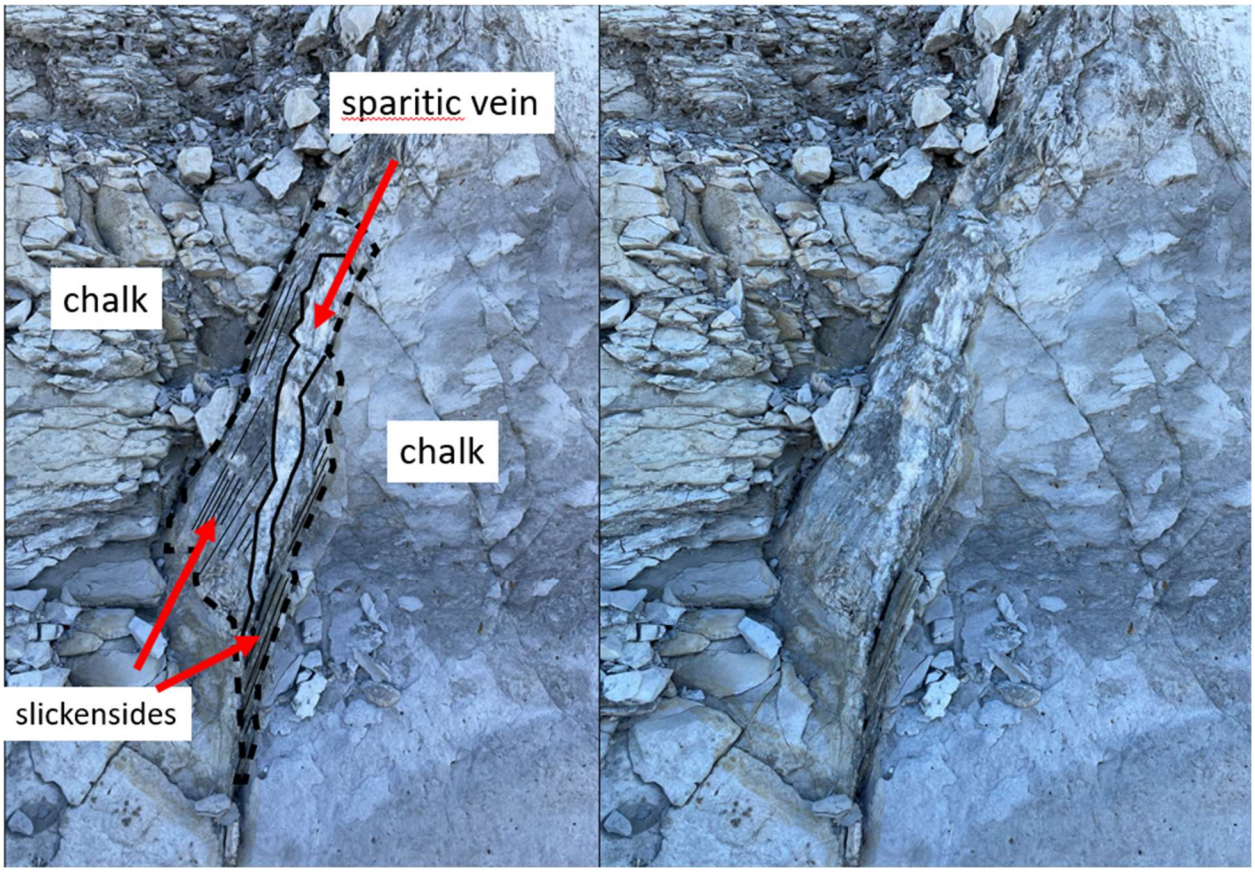

Field photo of a composite calcite vein with multiple generations of sparry calcite separated by striated boundaries. The composite veins form in asperities along the fault plane. Rock quarry road outcrop, looking into the wall.

Sparitic veins with multiple slickensides on both sides of the surfaces. Layering on its surface suggests at least five episodes of movements

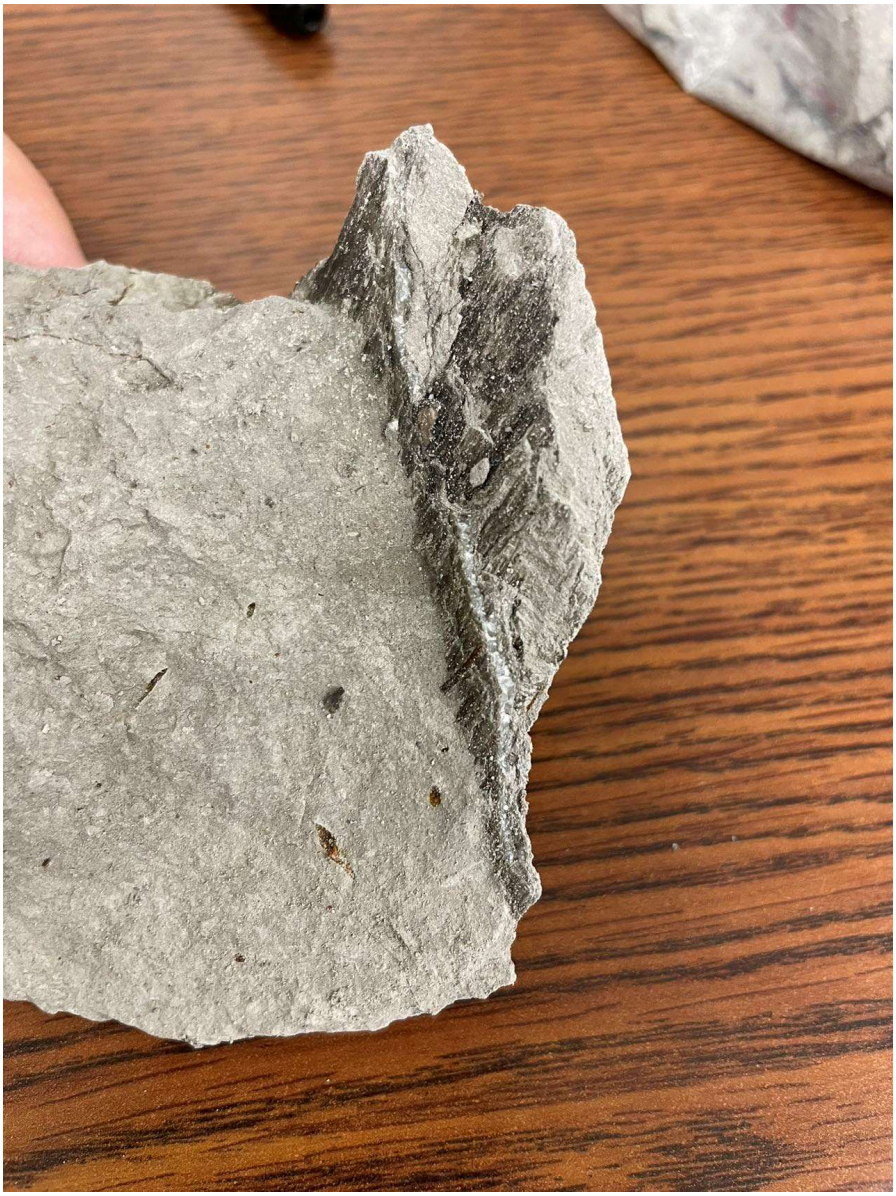

Image of multilayered calcite veins. The width of such vein is very small (less than a centimeter).

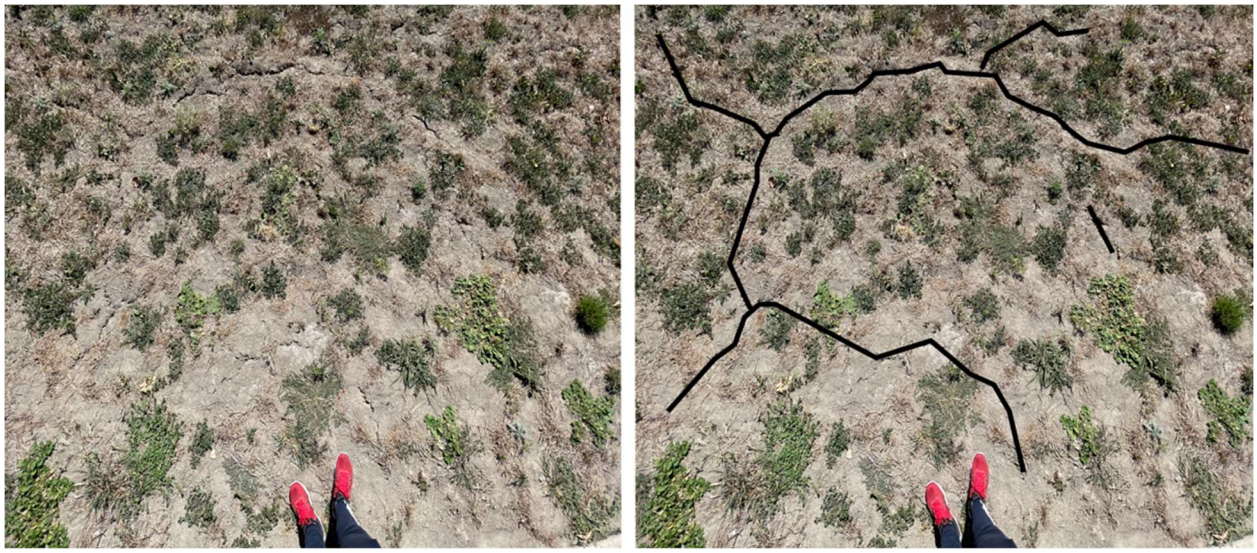

Naturally formed mudcracks on the floodplain of White Rock Creek. These cracks have thickness in the scale of decimeters and the polygon area is in the scale of square meter. Cracks are marked by black solid lines.

White Rock Creek overbank deposit collected in the field. The sediment is unsorted and forms an orthorhombic pattern. Fractures in the horizontal orientations seem to form earlier than those in the vertical direction.

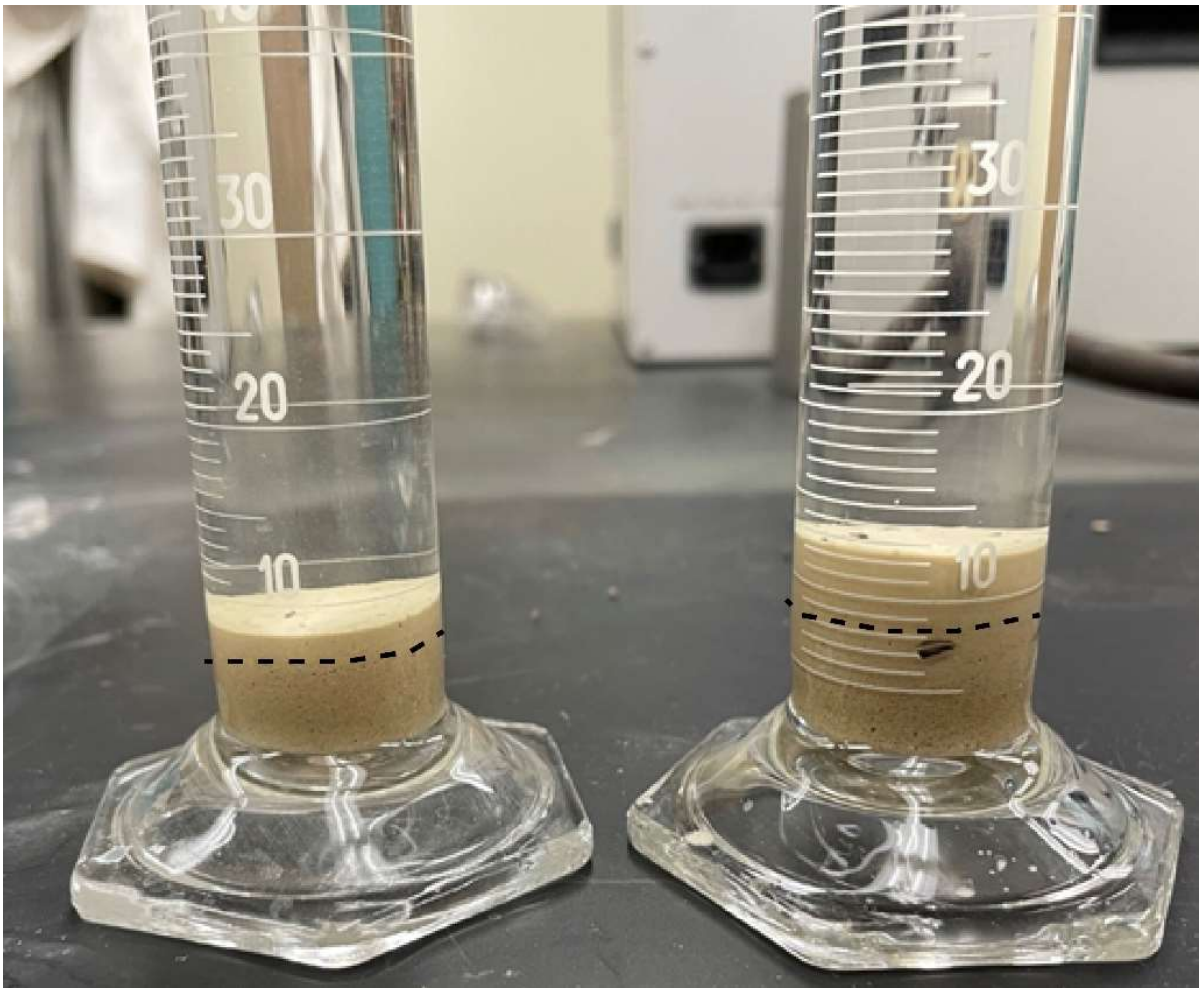

Grain size analysis of Austin Chalk debris and Bentonite mixture using graduated cylinders. Cylinder on the left contains material taken on the portion where fractures form hexagonal pattern in the tray and sediments in the right cylinder is taken from the center of the tray where cracks form irregular pattern. The black dashed lines are the inferred boundaries between the sand size and silt size material, which show that the percentage of fine grain material on the right is much higher than that on the left. Thus, the percentage of bentonite on the materials in the center of the tray is higher than the materials on the sides.

Cracks formed in 94% silica sand(500.98g) and 6% bentonite(30g). Only one continuous fracture formed on the center of the tray and it forms triple junctions with its branches.

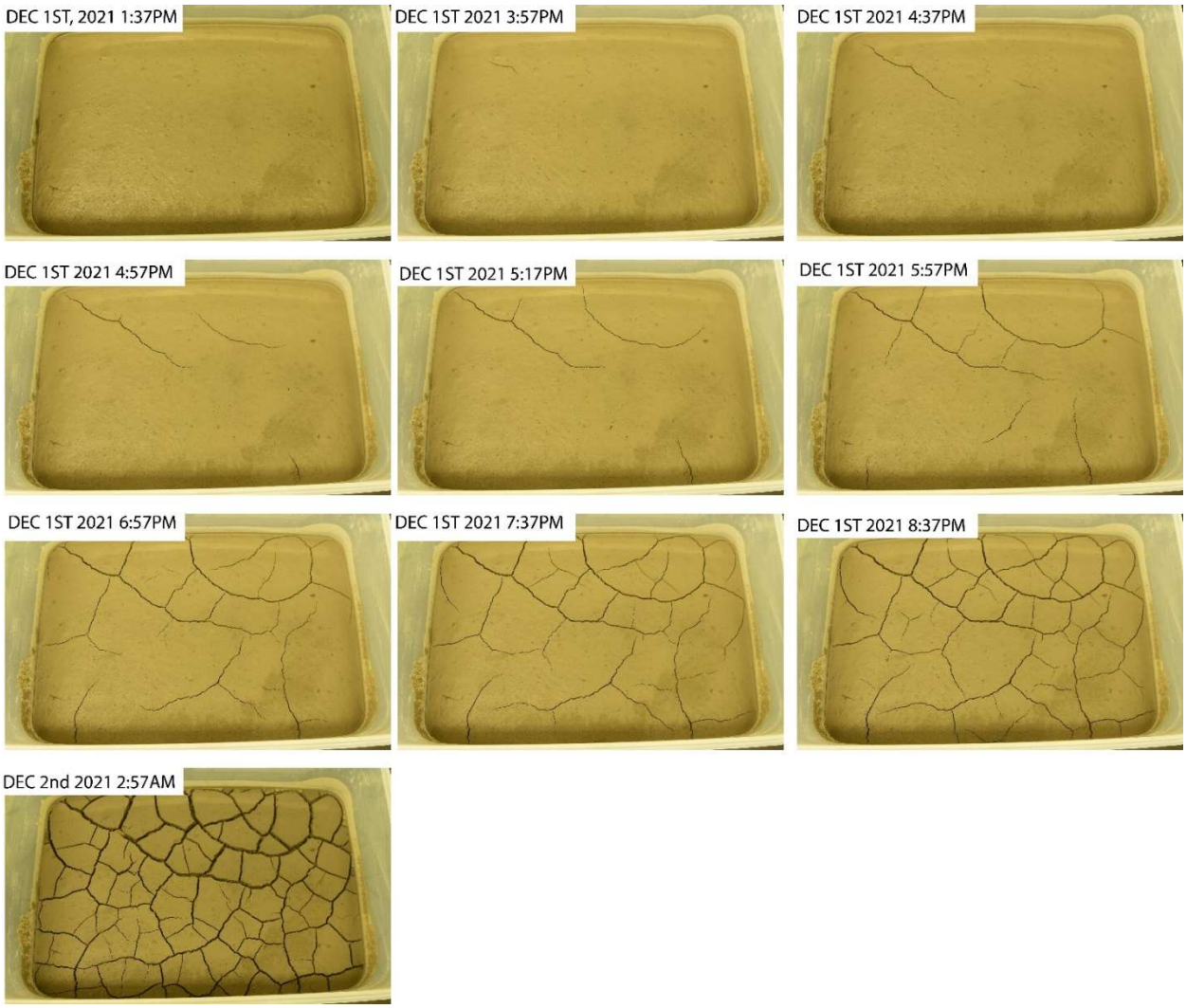

Series of images showing the development of desiccation cracks on 0.9cm thick White Rock Creek deposit.

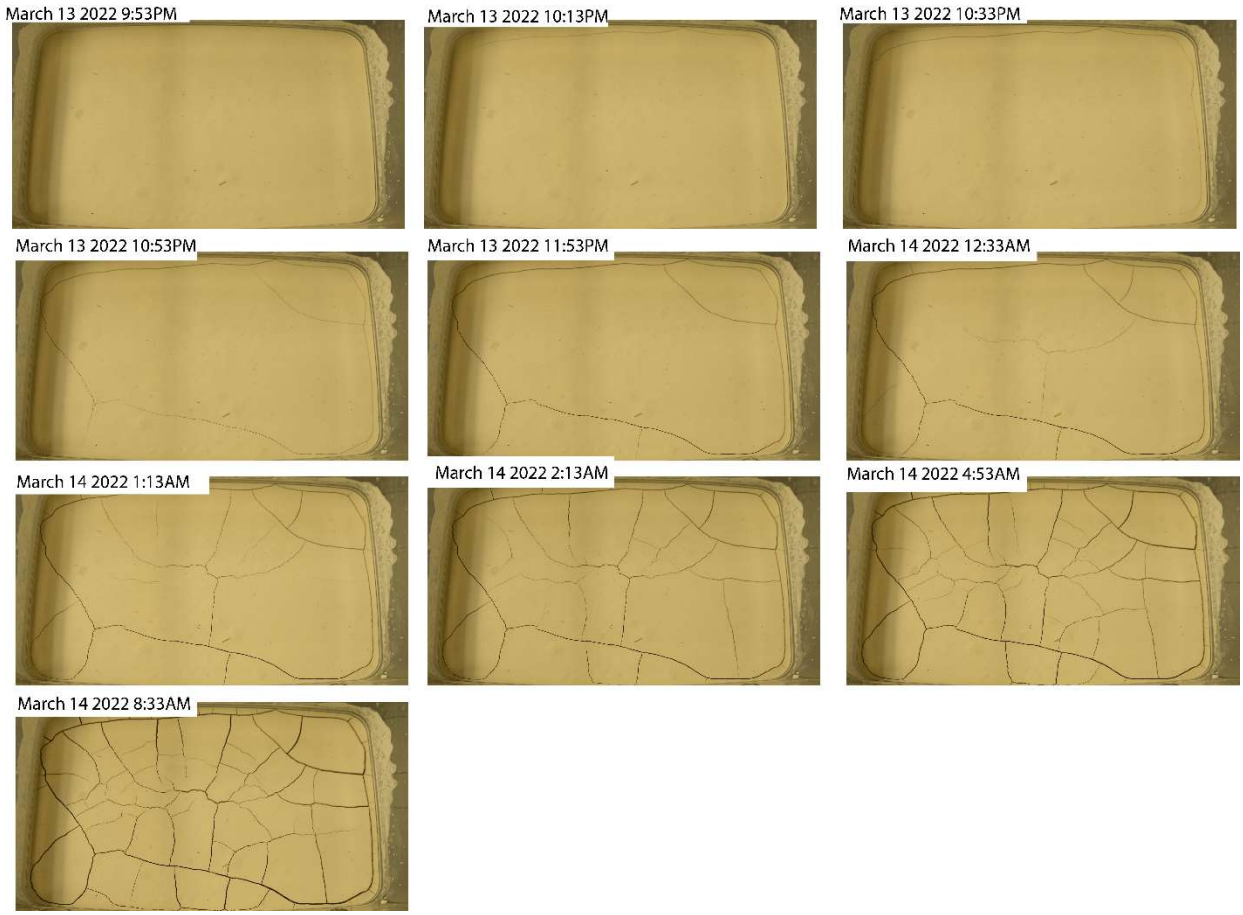

Series of images showing the development of desiccation cracks on calcareous sediment.

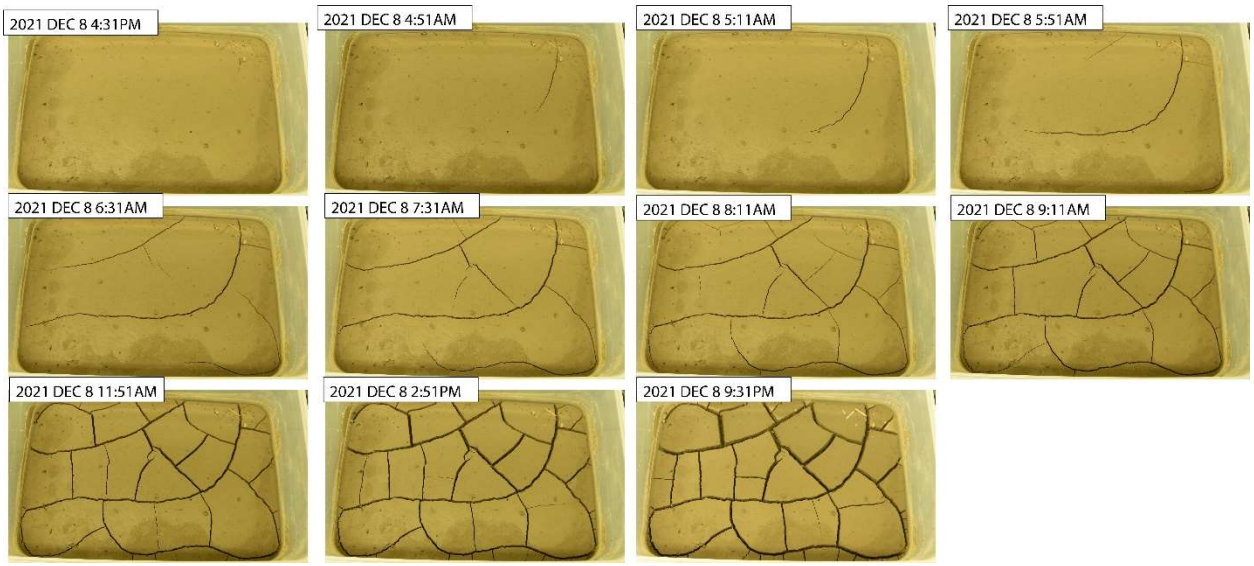

Series of images showing the development of desiccation cracks on 1.5cm thick White Rock Creek deposit

APPENDIX C

Drainages over the Eagle Ford Shale Formation in Irving quadrangle

Drainages in the Irving quadrangle overlay the quaternary deposit and the eagle ford shale formation. In this region, the shape of the drainages implies strong fracture control because streams form a rectangular pattern, especially in the west portion of the map, where streams form 90° angles. Plotting the drainages into the rose diagrams on both the drainages in the USGS topo maps and the first order streams show that streams over Irving quadrangle are grouped into two major directions striking at N-S and E-W, with an intersection angle close to 90°. Thus, if these drainages reflect the underlying fracture orientations, it will imply that the fracture pattern is orthorhombic. However, such rectangular pattern is absent in drainages at other quadrangles that contains Eagle Ford Shale formation, and the satellite image indicates that some streams in the Irving quadrangle are artificially modified. Therefore, the stream pattern in Irving might not truly reflect the fractures within the Eagle Ford Shale.

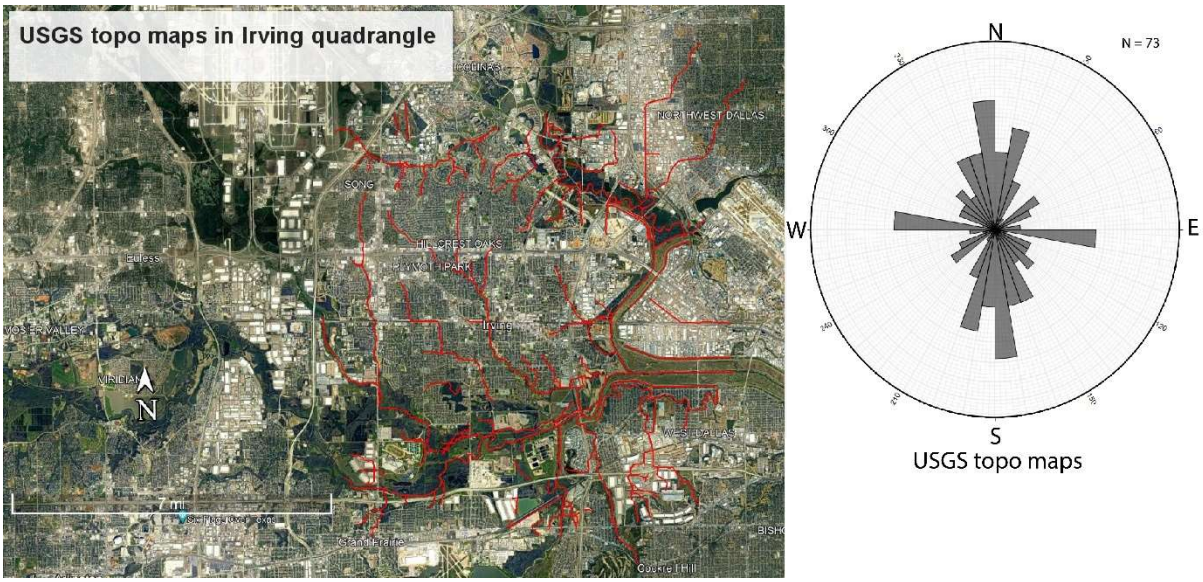

Satellite image overlain by the drainages over Irving quadrangle. The underlying formation is the Eagle Ford Shale. Some rectangular streamlines in the image follow the direction of roads, which indicates impact of human factors.

Drainages over the Duncanville and Oak Cliff quadrangles

The Duncanville and Oak Cliff quadrangles in Dallas County are located south of the trinity river, and the Austin Chalk escarpment mainly covers their surface. Previously, Blakemore (1939) studied the drainage pattern over the escarpment in this area and concluded that faults trending N10°W exert dominant control, and the joints at N65°E have a secondary effect on the drainages at the face of the escarpment. By comparing Blackmore's fracture data with the drainage data, we noticed that the dominant directions for the first-order streams fit the dominant trend of local faults and joints. On the other hand, the USGS drainages show two additional directions on the rose diagram: SE-NW at 110° and NNW-SSE at 150°. Therefore, it may suggest that small tributaries are more closely related to the fracture orientations in this area. Furthermore, the two additional orientations in the drainages over the USGS topo maps are parallel to the dip direction of the escarpment in this area, suggesting that the higher order streams fit the topography.

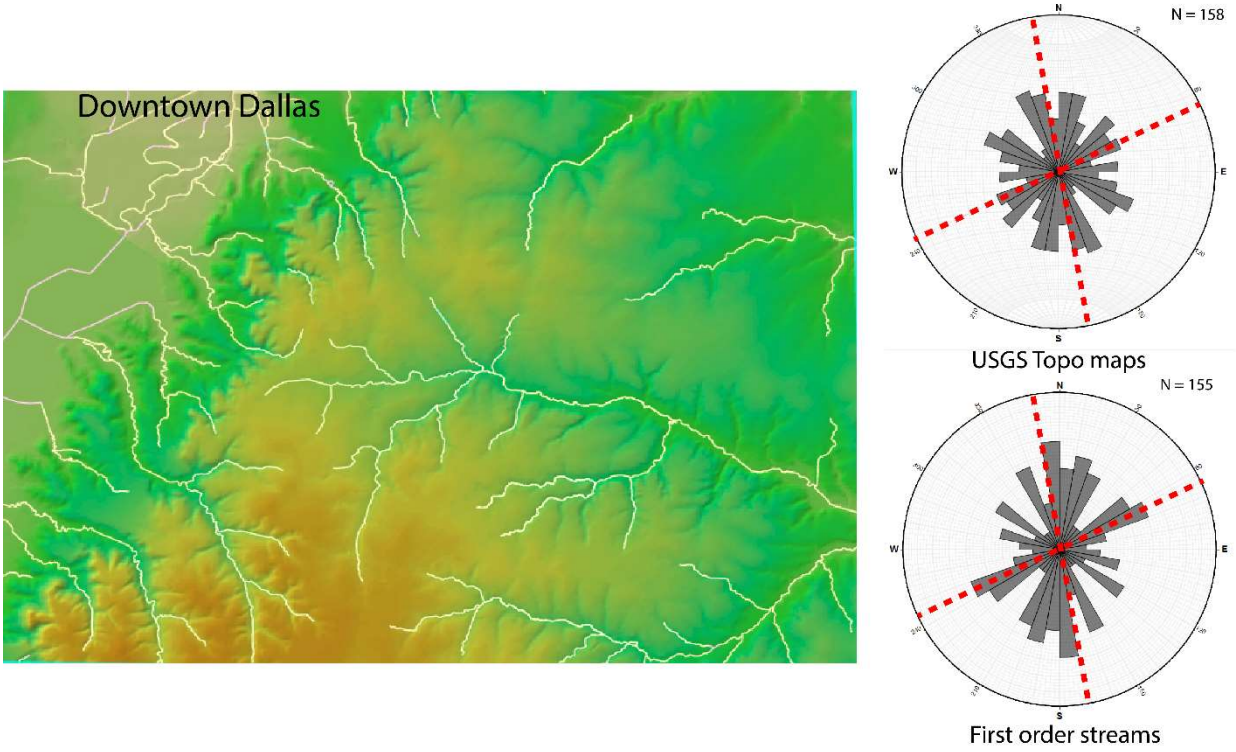

Map on the left shows USGS topo maps drainages over elevation maps of Duncanville and Oak Cliff quadrangles. Green color represents relatively low elevation and orange color represents relatively high elevation. Rose diagrams on the right are drainages in the USGS topo maps and first order streams, respectively. Red dashed lines represent the two dominant directions of faulting and jointing noticed by Blackmore (1939).

Drainages over Southwest Texas

Previous measurements found two dominant directions for faults and joints in the Eagle Ford Shale outcrop in southwest Texas (Ferrill et al., 2014; Gottardi and Mason, 2018). Faults dominantly strike in a northeast-southwest direction at 220°/40°, and a less abundant set of faults strike at 173.6°, making a dihedral angle of 50°. Joints are more abundant than the faults, and they strike at both 45° and 325°, making an almost 90° dihedral angle. Streams in both USGS topo maps and derived first order streams can flow in all directions, and the most dominant orientation is NE-SW, agreeing with the dominant fault and joint orientation as well as the downdip direction. Drainages may also reflect the N-S fault orientation, but this direction is not obviously dominant on the rose diagrams.

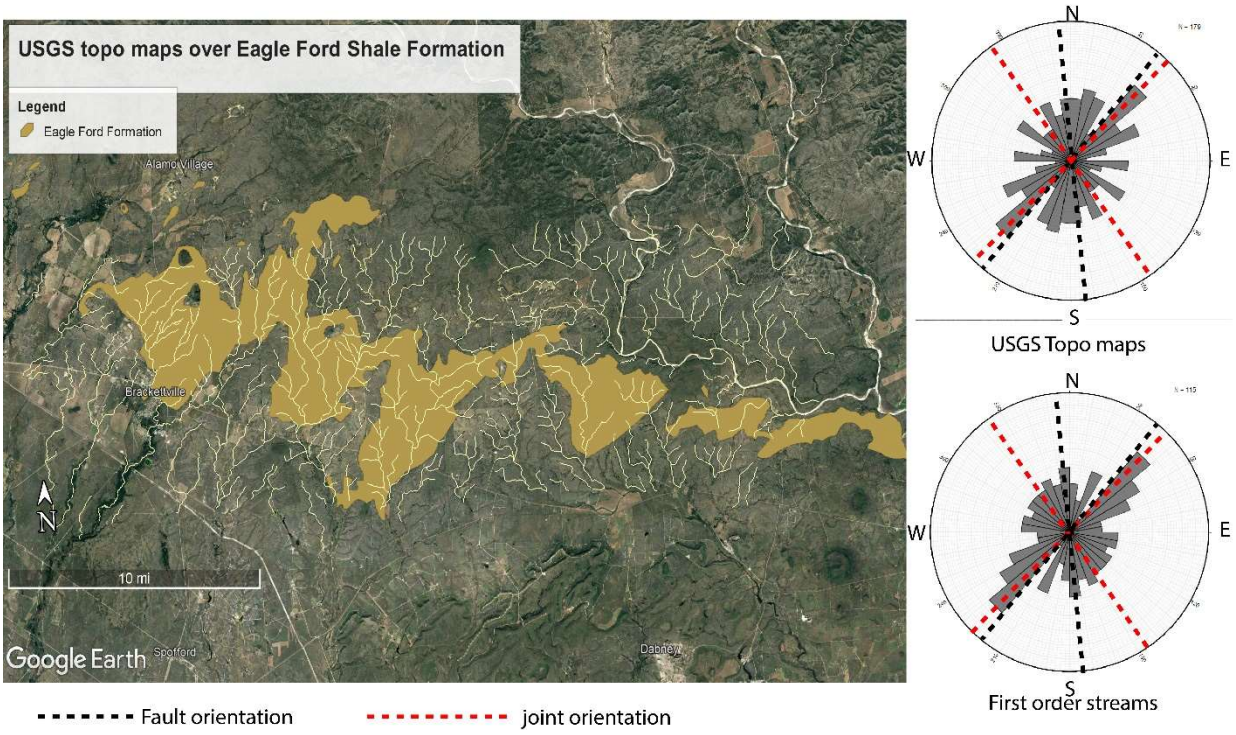

Map of Southwest Texas with drainages overlying the Eagle Ford Shale formation. The direction of streams in USGS topo maps and the derived first order streams are plotted as rose diagrams. Fault and joint orientations measured in previous studies on the Eagle Ford Shale outcrops in this region are labeled with black and red dashed lines.